Results in Engineering 32 (2026) 113039

Contents lists available at ScienceDirect

Results in Engineering

journal homepage: www.sciencedirect.com/journal/results-in-engineering

Research paper

Washcoated additively manufactured TPMS structures as catalytic converters for engines: A proof of concept

Fatemeh Mehdipour [a,*], Jan Erik Heinrich [a], Zexin Yu [b], Martin Kutscherauer [c], Michael Robert Tucker [d], Michael Rubin [a], Uwe Wagner [b], Thomas Koch [b], Roland Dittmeyer [a]

[a] Institute for Micro Process Engineering (IMVT), Karlsruhe Institute of Technology (KIT), Germany
[b] Institute of Internal Combustion Engines (IFKM), Karlsruhe Institute of Technology (KIT), Germany
[c] Institute for Chemical Process Engineering (CVT), Karlsruhe Institute of Technology (KIT), Germany
[d] Advanced Manufacturing Lab, ETH Zürich, Switzerland

ARTICLE INFO

Keywords:
Laser powder bed fusion
Triply periodic minimal surface
Washcoat
Catalytic converters
Exhaust-gas aftertreatment

ABSTRACT

Transitioning towards cleaner combustion technologies requires catalytic converters with high conversion efficiency, thermal stability, and low pressure drop. This proof-of-concept study evaluated additively manufactured triply periodic minimal surface (TPMS) architectures as catalytic carriers for exhaust-gas aftertreatment. The investigated set comprised eight stainless-steel TPMS monoliths based on Schwarz–diamond, gyroid, and Schwarz–primitive geometries in various orientations and a straight-channel reference monolith. All the monoliths were fabricated by laser powder bed fusion (PBF-LB/M), washcoated with 2 wt% Pt/γ-Al_2O_3, and tested using exhaust gas from a compressed natural gas engine. The carriers exhibited accurate external dimensions, continuous washcoat coverage, and low washcoat loss in adhesion tests. The TPMS architectures provided specific surface areas up to 1.65 mm^{-1}, compared with 0.82 mm^{-1} for the reference, while several configurations maintained pressure drops per unit length comparable to or lower than the reference monolith. The unrotated Schwarz–diamond structure with a 5 mm unit cell achieved the highest CO conversion of approximately 99 % and the highest washcoat-loading-normalised CO conversion, although this was accompanied by a comparatively high pressure drop. In contrast, the 10 mm gyroid configuration provided one of the most favourable conversion–pressure-drop balances. Under stoichiometric conditions (air–fuel equivalence ratio, $\lambda = 1$), the two highest-conversion TPMS configurations exceeded 90 % CO conversion, with simultaneous methane (CH_4) conversion and reduction of nitrogen oxides (NO_x) observed across the investigated TPMS configurations. Overall, the results indicate that TPMS topology, unit cell orientation, and specific surface area jointly affect catalyst utilisation and hydrodynamic resistance, highlighting the potential of additively manufactured TPMS catalyst carriers for advanced emission-control applications.

1. Introduction and motivation for using AM

Nitrogen oxides, carbon monoxide, and volatile organic compounds emitted by vehicles contribute significantly to ground-level ozone formation and photochemical smog, posing severe risks to human health and the environment. Since the 1970s, catalytic converters have been widely deployed to mitigate these pollutants [1]. These devices use a permeable, catalyst-coated channel network, commonly referred to as a catalyst carrier or catalyst substrate, to convert harmful emissions into less hazardous products such as CO_2, N_2, and H_2O [2]. Conventional carriers typically rely on ceramic honeycomb monoliths, which are valued for their high thermal stability and thermal-shock resistance. However, these ceramic matrices are inherently brittle and susceptible to mechanical failure under operational stresses such as vibrations and thermal gradients [3,4]. Furthermore, extrusion, the dominant manufacturing method, limits design complexity to simple square or hexagonal channels and restricts miniaturisation due to the material's plasticity constraints [5,6]. These geometrical limitations result in predominantly laminar flow and comparatively low external heat and mass transfer; furthermore, inlet flow maldistribution can lead to non-uniform cross-sectional velocity and temperature profiles during converter operation [7]. Cold-start conditions further reduce conversion

* Corresponding author.
E-mail address: fatemeh.mehdipour@kit.edu (F. Mehdipour).

https://doi.org/10.1016/j.rineng.2026.113039
Received 1 June 2026; Received in revised form 4 September 2026; Accepted 15 September 2026
Available online 19 September 2026

efficiency prior to reaching the catalyst light-off temperature [8,9]. Metallic monoliths have emerged as robust alternatives, offering superior mechanical strength, high thermal conductivity, and lower pressure drops via thin-walled channels that maximise geometric surface area [10,11]. The formability of metal foils facilitates the integration of corrugated or protruded flow-disturbing channel features, which disturb the near-wall flow and enhance external heat and mass transfer [11,12]. Nevertheless, the transient thermal response of metallic catalyst carriers remains dependent on substrate material, wall thickness, cell density, and overall thermal mass, which must be carefully balanced to ensure rapid light-off under transient exhaust conditions. Despite these advantages, conventional metallic and ceramic carriers remain restricted to simple geometries, typically sinusoidal or rectangular arrays, due to traditional manufacturing and economic limitations [13,14]. Additive manufacturing (AM) has relaxed these geometric constraints, enabling the fabrication of complex monolithic architectures with tailored porosity and surface topology [15]. Researchers have successfully demonstrated AM-fabricated ceramic and metal monoliths with enhanced catalytic and mass-transfer performance [16,17]. Among advanced cellular structures, open foams and lattice structures offer high surface areas and enhanced conversion efficiency, though they often suffer from excessive pressure-drop penalties [18,19]. To mitigate this surface-area–pressure-drop trade-off, triply periodic minimal surface (TPMS) geometries have gained attention. Their mathematically continuous, curved profiles lack sharp junctions and can provide high surface-to-volume ratios while promoting more uniform flow distribution, thereby supporting efficient heat and mass transfer with limited pressure-drop penalties [20,21]. Despite this progress, the practical implementation of washcoated, additively manufactured metallic structures remains limited, with applications largely confined to laboratory and pilot-scale model-gas investigations [22,23]. From an industrial perspective, advanced catalyst carriers must combine high catalytic effectiveness and low exhaust backpressure with reproducible manufacturing, washcoat compatibility, and mechanical and thermal durability. Additively manufactured TPMS architectures offer particular value where application-specific geometric optimisation justifies the additional manufacturing complexity [15,22]. However, broader industrial adoption requires validation of production scale-up, manufacturing throughput, long-term durability, and techno-economic viability [15,22]. The present engine-bench investigation therefore represents a step from geometry-focused laboratory studies towards application-oriented evaluation under real exhaust-gas conditions. Washcoating of additively manufactured metallic carriers presents specific technical challenges related to surface roughness, fluid wettability, coating homogeneity, and long-term adhesion under thermomechanical loading [24]. While a growing body of academic literature has investigated additively manufactured metallic monoliths for steady-state catalytic processes such as dry methane reforming, demonstrating competitive conversion rates and enhanced thermal profiles relative to conventional cordierite structures [25,26], previous literature has largely addressed these challenges in isolation. Prior studies have often focused on selected aspects such as parametric design, numerical flow analysis, manufacturing-route selection, model-gas catalytic testing, or simulation-based performance assessment. However, a comprehensive experimental evaluation that combines laser powder bed fusion (PBF-LB/M) of metallic TPMS substrates, washcoating of these carriers, assessment of washcoat adhesion, pressure-drop behaviour, and catalytic performance under real engine exhaust conditions remains scarce. The novelty of the present work lies in addressing this research gap through an integrated experimental assessment of metallic TPMS catalyst carriers produced by PBF-LB/M, spanning from substrate design and fabrication to washcoating, adhesion evaluation, pressure-drop characterisation, and engine-bench testing under real CNG exhaust-gas conditions. The primary objective of this study is to determine whether stainless-steel TPMS monoliths produced by PBF-LB/M can serve as manufacturable and washcoat-compatible catalyst carriers that improve the trade-off between pollutant conversion and pressure drop in CNG exhaust-gas aftertreatment. To achieve this, the secondary objectives focus on evaluating the manufacturability of distinct TPMS topologies fabricated as stainless-steel monoliths, characterising the Pt/γ-Al_2O_3 washcoat loading, thickness distribution, and mechanical adhesion on the AM surfaces, quantifying the pressure-drop characteristics of the investigated substrate geometries, and assessing the conversion of CH_4, CO, and NO_x under real CNG engine exhaust-gas conditions.

2. Digital design and geometric modelling of monolithic carriers

2.1. Parametric design of multichannel monoliths

Each monolith in this work consists of a cylindrical outer shell and a structured infill, forming a cylinder 50 mm in *height* and 23.88 mm in *diameter* that is designed to fit precisely within the sample holder of an engine test bench (see Section 3.5 for details). Previous work by Grinschek et al. [27] demonstrated that gas-tight stainless-steel thin walls with characteristic thicknesses in the range of 200–300 μm can be fabricated by PBF-LB/M. This range has thus been adopted in the present study as a design guideline. This manufacturing constraint played a decisive role in maximising the compactness of the designs. Stereolithography files were generated using nTop (version 4.25.2) computer-aided design software. Implicit modelling was employed to efficiently design periodic patterns of sheet-network TPMS configurations with an *iso-value* of $c = 0$, ensuring a continuous and interconnected topology. Schwarz–primitive, gyroid, and Schwarz–diamond geometries have previously been proposed as minimal-surface architectures for catalytic converter substrate concepts [20]. Therefore, they were selected as representative TPMS geometries in this work and parametrically modified in terms of unit cell size and orientation. These geometries are particularly relevant for catalytic substrates because their continuous and interconnected channel networks provide a high geometric surface area, avoid sharp junctions that may promote non-uniform washcoat accumulation, and support gas–surface interaction. In addition, the three selected unit cell types differ in channel connectivity, geometric tortuosity, and flow-path uniformity, enabling the influence of unit cell topology on manufacturability, washcoating, pressure drop, and catalytic performance to be assessed systematically. The implicit level-set equations defining the mid-surfaces of the Schwarz–primitive, gyroid and Schwarz–diamond TPMS geometries are given by Eqs. (1)–(3). The corresponding finite-thickness unit cells were generated from these periodic surfaces by applying the selected wall thickness and unit cell dimensions; representative unit cell geometries are illustrated in Fig. 1.

$$\text{Schwarz–primitive:}\quad \cos(x)+\cos(y)+\cos(z)=c \tag{1}$$

$$\text{Gyroid:}\quad \sin(x)\cos(y)+\sin(y)\cos(z)+\sin(z)\cos(x)=c \tag{2}$$

$$\text{Schwarz–diamond:}\quad \sin(x)\sin(y)\sin(z)+\sin(x)\cos(y)\cos(z)+\cos(x)\sin(y)\cos(z)+\cos(x)\cos(y)\sin(z)=c \tag{3}$$

The infill structures, featuring a *wall thickness* of 0.2 mm, were designed by varying: (1) the unit cell type, (2) the unit cell size, and (3) the unit cell orientation with respect to the primary fluid flow direction within the final monolith. Additionally, (4) a linear unit cell size gradient was introduced along the axial direction of the monolith (parallel to the fluid flow). It should be noted that these approaches were implemented *separately* in order to isolate the effect of each individual design parameter. The specific surface area (s_v) was determined by extracting the absolute surface area (S_{abs}) from nTop and normalising it by the corresponding total geometric volume (V_{total}). For the unit-cell characterisation in Table 2, V_{total} denotes the unit-cell volume, whereas for the monolith characterisation in Table 3, it denotes the total external volume of the 50 mm-long monolith. Porosity (Φ) and solid volume fraction (ϵ_s) were subsequently calculated using Eqs. (4b) and (4c),

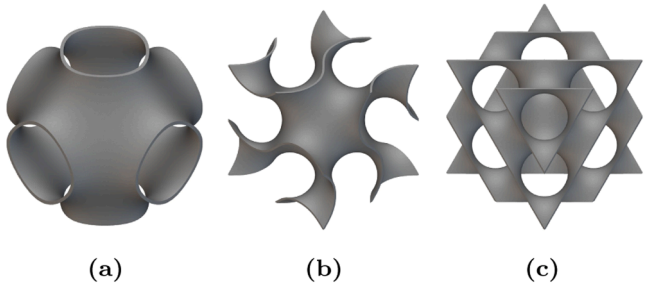

Fig. 1. Isometric view of representative finite-thickness sheet-network TPMS unit cells generated from the implicit level-set surfaces. (a) Schwarz–primitive, (b) gyroid and (c) Schwarz–diamond, corresponding to Equations 1–3, respectively.

respectively, where V_{void} and V_{solid} denote the void and solid volumes of the unit cell:

$$s_v = \frac{S_{\text{abs}}}{V_{\text{total}}} \tag{4a}$$

$$\Phi = \frac{V_{\text{void}}}{V_{\text{total}}} = \frac{V_{\text{void}}}{V_{\text{solid}} + V_{\text{void}}} \tag{4b}$$

$$\varepsilon_s = 1 - \Phi \tag{4c}$$

2.1.1. Monolithic designs via unit cell modifications

Parametric and topological modifications were employed to generate distinct unit-cell-based variations, with each modification applied independently in order to isolate the influence of individual geometric parameters on the resulting integrated architecture. In the following, TPMS-based monoliths are denoted as $XX_{a,b}$, where XX identifies the surface type (GY: gyroid, SD: Schwarz–diamond, SP: Schwarz–primitive), a represents the unit cell side length in millimetres ($a = 5$ or $a = 10$), and b specifies the orientation (s: standard, e: edge, c: corner). For instance, $SD_{5,s}$ denotes a monolith filled with Schwarz–diamond unit cells with a side length of 5 mm in a standard-positioning pattern.

The gradient-based designs, $GY_{\text{G1,s}}$ and $GY_{\text{G2,s}}$, represent gyroid-filled monoliths in a standard orientation incorporating continuous, linear gradients in unit cell size along the axial direction. As illustrated in Fig. 2, the G1 gradient maintains a constant unit cell height ($z = 10$ mm), while the cross-sectional dimensions decrease linearly from 10 mm × 10 mm at the inlet to 5 mm × 5 mm at the outlet. Similarly, the G2 gradient follows an identical cross-sectional reduction but employs a uniformly compressed unit cell height ($z = 5$ mm) throughout the entire monolith length.

In Fig. 3, each row corresponds to one TPMS type, while columns (a)–(d) show cross-sectional CAD renderings of monoliths generated using different unit cell size and/or orientation variants.

- Type: Using *isometric* unit cells with a *side length of* 10 mm, the three monoliths illustrated in Fig. 3(a) were constructed. Here, only the unit cell type was varied, while the *size* and *orientation* were kept *constant*.
- Size: While keeping the *type constant* and *without* applying *rotation*, the unit cell size was adjusted to enable additional design variations. Fig. 3(d) shows a finer internal structure characterised by reduced fluid passage dimensions and smaller channel openings resulting from the higher packing density, achieved by transitioning from an initial dimension of 10 mm (Fig. 3(a)) to a reduced size of 5 mm.
- Orientation: With the *type* and *size* fixed, the unit cell was rotated about its principal axes prior to periodic expansion. This rotation was intended to modify the *open frontal area*, *tortuosity*, and consequently the associated *pressure drop*. The monoliths shown in Fig. 3(a), (b), and (c) were generated using (i) *standard* positioning, (ii) a 45° rotation about the x-axis (*edge* positioning), and (iii) a combined rotation of 45° about the x-axis and 35.25° about the y-axis (*corner* positioning), respectively.
- Size Gradient: To investigate the influence of a gradual variation in the unit cell size, two *gyroid* structures incorporating a linear gradient in unit cell size were designed. Fig. 2 illustrates these configurations. Both designs feature a transition from a 10 mm × 10 mm unit cell cross-section to a 5 mm × 5 mm cross-section. The only difference between them lies in the unit cell height: one design incorporates a height of 10 mm, while the other uses 5 mm.

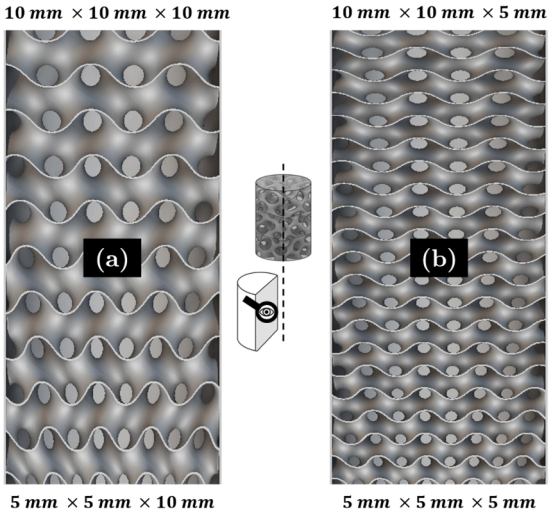

Fig. 2. Implementation of linear unit-cell size gradients to gyroid-based monoliths. The left and right configurations correspond to (a) $GY_{G1,s}$ and (b) $GY_{G2,s}$, respectively. The unit-cell at the top has dimensions of ($GY_{G1,s}$: $x_1 = 10$ mm, $y_1 = 10$ mm, $z_1 = 10$ mm; $GY_{G2,s}$: $x_1 = 10$ mm, $y_1 = 10$ mm, $z_1 = 5$ mm) and gradually decreases in size to ($GY_{G1,s}$: $x_2 = 5$ mm, $y_2 = 5$ mm, $z_2 = 10$ mm; $GY_{G2,s}$: $x_2 = 5$ mm, $y_2 = 5$ mm, $z_2 = 5$ mm) at the bottom.

The structural variations introduced by rotating and scaling the unit cells are compiled in Fig. 3. The figure presents a dual visual representation of the design variations: the leftmost column displays UV-illuminated photographs of individual stereolithography (SLA)-printed unit cells, manufactured specifically to clearly visualise their underlying topologies (Schwarz–primitive, gyroid, and Schwarz–diamond). Columns (a)–(d) present cross-sectional CAD renderings of the integrated monoliths viewed along the primary flow direction in order to illustrate the internal fluid-passage structures resulting from the different spatial configurations.

2.2. Tortuosity calculation for unit cells

In laminar and low-superficial-velocity flow regimes, viscous wall friction dominates, and the pressure drop is strongly influenced by tortuosity (τ), since winding flow pathways increase the effective channel length and wall–fluid interaction [28]. In the investigated TPMS channel networks, changes in flow direction, local constrictions, and variations in channel connectivity may additionally affect local velocity distribution and transverse transport. These geometry-induced effects are considered here qualitatively, rather than as a fully resolved flow-mechanistic description. Therefore, the tortuosity-based approach employed here serves as a useful geometric indicator for the comparative evaluation and preliminary screening of the pressure-drop behaviour of the different monolithic topologies prior to manufacturing. Geometric tortuosity (Eq. (5)) is defined as the ratio of the effective flow path length (l_{eff}) to the corresponding direct distance (l_0) along the investigated transport direction.

$$\tau = \frac{l_{\text{eff}}}{l_0} \tag{5}$$

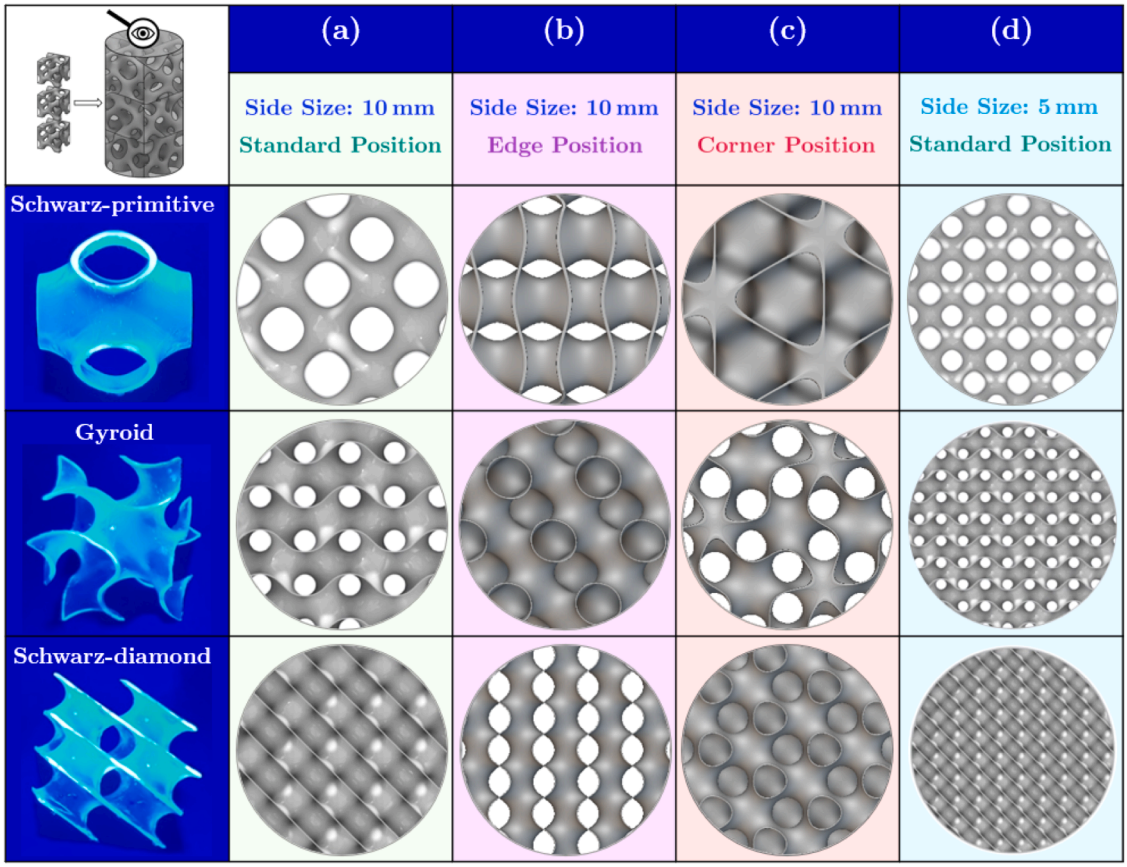

Fig. 3. Photographs of individual unit cells and cross-sections of the monolithic designs. The leftmost column shows UV-illuminated photographs of individual SLA-printed unit cells illustrating the underlying TPMS topologies. Columns (a)–(d) present numerical cross-sectional renderings of the corresponding integrated monolithic structures. Structural variations were introduced through systematic rotation and scaling of the unit cells.

In the present work, τ is not evaluated from individual point-to-point trajectories or streamlines. Instead, it is defined as an effective, direction-dependent transport tortuosity[1] of the connected void/channel domain of the TPMS unit cell. For each investigated coordinate direction, the two opposing faces normal to that direction are treated as the reference inlet and outlet planes. The direct distance l_0 corresponds to the face-to-face distance between these planes, i.e. the unit cell length in the investigated direction. The effective length l_{eff} is not measured for individual starting points; rather, it is inferred indirectly from the reduction in the integrated heat-transfer rate through the TPMS channel domain relative to an equally sized straight reference control volume. Therefore, the reported tortuosity represents a volume-averaged effective quantity over all accessible transport paths between the two opposing faces. While this definition is geometrically intuitive, the effective pathway l_{eff} in complex channel networks is not uniquely defined, as local transport paths vary across the channel cross-section. To calculate the tortuosities of the applied unit cells, the methodology proposed by Cooper et al. [29] was followed. This approach, illustrated in Fig. 4, estimates an effective tortuosity using a heat-transfer analogy, providing a computationally convenient proxy by relating deviations in heat flux through the internal channels to those of an equivalent straight control volume. The resulting temperature field reflects the available transport pathways within the geometry, such that more complex structures lead to longer and more indirect heat transfer paths, analogous to increased effective flow path lengths. Within this framework, the connected void/channel domain of the unit cell is treated as a conducting medium with adiabatic outer boundaries and uniform thermal conductivity. A temperature gradient is established in one direction by prescribing constant, arbitrary temperatures to two opposing, parallel faces. In their standard orientation, TPMS unit cells exhibit cubic isotropy, meaning their geometric tortuosities along the x, y, and z coordinate axes are identical. Spatial rotation breaks this symmetry, leading to direction-dependent variations in heat transfer. Therefore, in this study, directional tortuosity values were evaluated along all three orthogonal coordinate axes (x, y, and z) in order to capture these orientation-dependent variations. The steady-state heat-transfer rate through the accessible channels ($\dot{Q}_{\text{channels}}$) was calculated numerically along the investigated axis using the Finite Volume Method to solve Fourier's law, given in Eq. (6):

$$\nabla \cdot \left(-k_f \nabla T\right) = 0 \tag{6}$$

Here, k_f denotes the thermal conductivity of the fluid. To determine the tortuosity, the heat transfer rate within the open channels of the unit cell must be compared to that of a reference control volume with identical dimensions ($\dot{Q}_{\text{CV}}$) and the same thermal conductivity. The quantity $\dot{Q}_{\text{CV}}$ is calculated using Eq. (7):

$$\dot{Q}_{\text{CV}} = -A k_f \frac{\Delta T}{L} \tag{7}$$

In this expression, A represents the cross-sectional surface area and L denotes the length of the cubic control volume. Based on the heat transfer rates $\dot{Q}_{\text{CV}}$ and $\dot{Q}_{\text{channels}}$, the tortuosity can be estimated with Eq. (8):

$$\tau = \Phi \frac{\dot{Q}_{\text{CV}}}{\dot{Q}_{\text{channels}}} \tag{8}$$

[1] Effective tortuosity refers to the ratio of the volume-averaged fluid path length to the straight-line distance across the unit cell, calculated via the heat-transfer analogy described in this section.

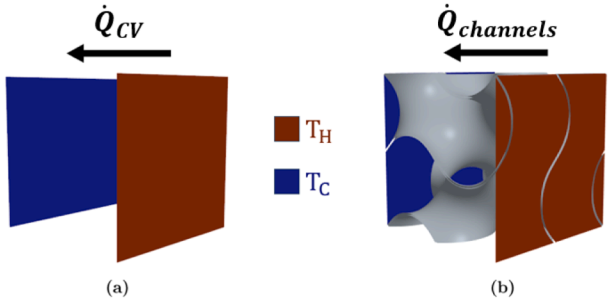

Fig. 4. Heat-transfer analogy for effective tortuosity estimation. (a) Reference control volume used to compute $\dot{Q}_{CV}$. (b) Open-channel gyroid unit cell used to compute $\dot{Q}_{channels}$ through the connected void/channel domain.

In this equation, Φ represents the porosity of the unit cell. This formulation is consistent with the non-uniformity of local transport paths in complex channel geometries.

3. Experimental procedure

3.1. Manufacturing and post-processing of the monoliths

The investigated geometries were generated using a parametric design approach, allowing systematic variation of unit cell size and orientation while targeting a high specific surface area and a sufficiently large open frontal area. Using RDesigner slicing software, the monolithic geometries were oriented with their cylindrical axes vertically aligned with the build-platform z-axis for support-free fabrication and scan-path generation. A gas-atomised stainless steel 316L powder (Carpenter Additive, PowderRange 316LF) with a particle size range of 15–45 μm was used for printing on an SLM DMG Mori Realizer 125 machine. The PBF-LB/M process parameters were a layer thickness of 50 μm, a hatch laser power of 115 W, and a boundary laser power of 110 W. The hatch and boundary scan speeds were 1000 and 200 mm s^{-1}, respectively, and the spacing between adjacent laser lines was 80 μm. For each investigated TPMS monolith design, three nominally identical samples were fabricated and subsequently subjected to the same washcoating procedure. The monoliths were intentionally printed with an excess axial length of 55 mm to provide sufficient allowance for subsequent electrical discharge machining (EDM) separation and final length adjustment. After printing, the build chamber was allowed to cool down before the printed components were carefully extracted. Excess unsintered powder was removed using a brush and compressed air. To ensure complete removal of remaining loose powder from the internal channels, ultrasonic cleaning was performed in water at room temperature for at least 2 h. Finally, the monoliths were separated from the build platform using CNC wire-cut EDM (AGIE-CUT 100) in order to minimise mechanically induced deformation during removal and to adjust the samples to their final length. This was particularly important because force-based removal could distort the circular outer cross-section of the thin-walled monoliths into an oval shape. After EDM separation, the final sample height and external diameter were measured to verify dimensional compatibility with the engine-test sample holder.

3.2. Catalytic washcoating

The preparation of the stabilised catalyst suspension and the washcoating procedure are based on a coating methodology optimised in a separate study, which will be reported elsewhere. The essential operating conditions relevant to the present work are summarised here. The washcoating procedure consisted of four key stages: surface pretreatment, dipping-and-withdrawing sequences, spin-drying, and calcination. To remove potential surface contaminants and ensure pristine substrates prior to washcoating, an additional ultrasonic cleaning step in isopropyl alcohol (IPA) was performed (Elma Elmasonic X-tra 50H, 160 W, 30 min, ambient temperature). Residual IPA was subsequently removed using compressed air, followed by a pre-oxidation treatment in a muffle furnace (Thermo Scientific M110, 800 °C, 5 h). A suspension containing 2 wt% Pt supported on γ-Al_2O_3 was prepared and used as the catalytic phase for deposition onto the PBF-LB/M-fabricated metallic monoliths. Pt/γ-Al_2O_3 was selected because Pt is a well-established noble-metal active phase for CO oxidation and exhaust-gas aftertreatment. The Pt loading of 2 wt% was used as a representative fixed catalyst formulation, consistent with Pt-based alumina washcoat formulations used in structured emission-control catalyst studies [30]. In the present work, the noble-metal loading was kept constant for all samples. This was done to isolate the influence of monolith geometry on washcoating, pressure drop, and catalytic performance, rather than to optimise the catalyst formulation itself. Specifically, 2.25 g of the Pt/γ-Al_2O_3 catalyst powder was dispersed in 35 mL of isopropanol together with 11.1 wt% Sasol Disperal P2, relative to the catalyst powder mass, as a highly dispersible pseudo-boehmite (AlO(OH)) binder. The resulting mixture was homogenised by planetary ball milling at 500 rpm for a total milling time of 35 min using zirconia grinding media. This formulation and preparation protocol produced a stable slurry with a median particle size of $d_{50,3} \approx 200$ nm, as verified by dynamic light scattering, thereby preventing rapid phase separation and promoting the formation of uniform washcoats throughout the complex channel structures of the printed monoliths. Each sample was subjected to twelve consecutive immersion steps in the washcoating suspension, with an intermediate spin-drying step applied after each immersion. For the highly compact $SD_{5,s}$ geometry, the standard 12-cycle procedure led to excessive washcoat accumulation; therefore, an adjusted 10-cycle procedure was used for the replicate values included in the statistical evaluation and for selection of the engine-test sample, as detailed in Appendix C. Following the final washcoating sequence, the monoliths were calcined at 500 °C for 5 h in a muffle furnace (Thermo Scientific M110). Each sample's mass was recorded using a precision balance (Kern ABJ 220-4M) before dip-coating, after the intermediate drying stages, and after final calcination. The resulting washcoat loading was determined from the mass gain after calcination relative to the initial mass prior to washcoating. Washcoat-loading statistics were based on three independently prepared samples for each geometry, except for $SD_{5,s}$, for which two samples were included (further details are provided in Appendix C). Accordingly, the corresponding standard deviations represent sample-to-sample variation between independently prepared samples.

3.3. Washcoat evaluation

This research assessed washcoat adhesion (stability) and washcoat-thickness distribution (uniformity) in TPMS-based geometries using adhesion tests and microscopic analysis. Elemental composition and spatial distribution of the washcoat were examined using wavelength-dispersive X-ray spectroscopy (WDX). Washcoat thickness was determined via cross-sectional SEM imaging, while adhesion was assessed through both drop and ultrasonic tests.

3.3.1. Adhesion testing and thickness distribution

Adhesion was assessed using two destructive methods to evaluate the stability of the washcoated layers under different mechanical stresses. Initially, samples were dropped from a known height (111.5 cm) onto a linoleum surface to determine the mass loss Δm_1 (g), as defined in Eq. (9), representing impact-induced damage. To simulate more severe conditions involving vibrational effects, the same samples subsequently underwent ultrasonic treatment at a power of 160 W for 30 min at room temperature to determine Δm_2 (g), as defined in Eq. (10).

$$\Delta m_1 = m_{\text{before drop}} - m_{\text{after drop}} \tag{9}$$

$$\Delta m_2 = m_{\text{after drop}} - m_{\text{after ultrasonic exposure}} \tag{10}$$

Endoscopic imaging was employed to qualitatively assess the spatial distribution of the washcoat layers within the monoliths. Detailed quantitative characterisation was subsequently carried out using cross-sectional SEM micrographs acquired at a magnification of 250×. Images were obtained at three distinct axial positions of each sample: one end face (End A), the mid-length position, and the opposite end face (End B). At each axial position, the reported mean washcoat thickness and standard deviation were calculated from 18 local thickness measurements along the analysed SEM cross-section. The standard deviations therefore represent local thickness variations within the corresponding cross-section. The End A/End B designation is arbitrary and serves solely to define an axial coordinate, as the samples were rotated between successive coating cycles and did not possess a fixed inlet or outlet during processing.

3.4. Pressure drop experiments

The monolithic samples were securely mounted in a custom sample holder connected upstream to an extension pipe with an internal diameter matching the external diameter of the sample, thereby ensuring uniform flow conditions and minimising inlet flow disturbances. Compressed air at a constant pressure of 6.5 bar was supplied to a mass flow controller (Brooks Instruments Model 5878) to regulate the flow at discrete normal volumetric flow rates of 1.56, 3.15, 4.73, and 6.36 $\mathrm{Nl\,min^{-1}}$. These values correspond to uniform increments in the nominal volumetric gas flow rate under standard reference conditions (0 °C and 1.013 bar). The non-rounded appearance of these values arises from the conversion between the controller setpoints and the normalised flow representation, rather than from arbitrary experimental selection. Based on the full frontal cross-sectional area of the monoliths, calculated from the common outer diameter of 23.88 mm, these normal volumetric flow rates correspond to superficial gas velocities under standard reference conditions of 0.058, 0.117, 0.176, and 0.237 $\mathrm{m\,s^{-1}}$, respectively. The superficial velocity was calculated using the projected frontal area of the monolith rather than the geometry-dependent open frontal area, thereby providing a consistent basis for comparison between the different TPMS topologies and the straight-channel reference. Superficial velocity was used as the comparative flow descriptor rather than a Reynolds number because a single representative hydraulic diameter is not uniquely defined for the investigated TPMS channel networks and varies with topology, unit cell size, and orientation. Although the investigated monolith topologies differ in open frontal area and internal void volume available for gas transport, the use of identical imposed normal volumetric flow rates and a common frontal cross-sectional area allows the hydrodynamic and pressure-drop behaviour to be compared under the same superficial flow conditions at each imposed flow rate. The pressure difference across the sample holder was measured using a calibrated differential pressure transducer (Wika air2guide A2G-45, range 0–2500 Pa, accuracy ±1.5 % of full scale), while the outlet stream was vented directly to the atmosphere. For each imposed flow condition, the pressure-drop measurement was repeated three times on the same specimen under identical experimental conditions. The reported pressure-drop values correspond to the mean values of these three repeated measurements ($n = 3$), and the corresponding standard deviations were calculated. For several data points, the standard deviations were smaller than the marker size and are therefore not visually distinguishable. Initial baseline measurements were conducted using 50 mm-long monolith configurations representative of the engine-test geometry. These preliminary measurements included both coated and uncoated 50 mm samples. However, the resulting pressure differentials were close to the practical resolution of the measurement setup, making reliable discrimination between the investigated topologies difficult. To enhance measurement sensitivity and ensure reproducible quantification of the hydrodynamic differences, the experiments were therefore extended to monolithic substrates with a length of 150 mm, thereby increasing the measurable pressure drop across the investigated flow range. The 150 mm samples were tested without washcoat in order to isolate the geometry-induced contribution of the channel architecture to the pressure-drop behaviour and to avoid additional variability from coating thickness or local coating distribution. Accordingly, the resulting pressure-drop data provide a comparative hydrodynamic screening of the investigated topologies and establish geometry-dependent trends for interpreting the conversion–pressure-drop trade-off.

3.5. Engine tests

Engine tests were conducted using the test setup shown in Fig. A.1, a three-cylinder compressed natural gas engine with a displacement of 2.19 L (bore/stroke: 92 mm × 110 mm), delivering 42 kW of rated power and a maximum torque of 160 N m. A dynamometer enabled controlled braking, while engine speed and load were continuously monitored. Intake air was supplied by a compressor delivering dry air with adjustable pressure, allowing turbocharging conditions to be simulated. A back-pressure valve was installed in the exhaust line to reproduce turbine-equivalent exhaust conditions. The exhaust system was designed to accommodate small-diameter catalytic converters under conditions comparable to those of a full-scale catalyst. The samples were mounted in a bypass line branching downstream of the exhaust manifold and held in a dedicated sample holder. For each geometry, one representative coated monolith was selected from the available replicate coated samples and used for engine-bench testing. The replicate coated samples were used to assess washcoat-loading reproducibility, whereas the catalytic conversion data correspond to the selected engine-test sample for each geometry. Gas flow rate and temperature in the bypass, and thus the gas hourly space velocity (GHSV), were controlled by a flow regulation valve and a thermally controlled heating sleeve surrounding the exhaust bypass duct, ensuring that the boundary conditions at the sample matched those at the reference position. Exhaust mass flow rate was measured with a DeltaFlow DF8 mass flow meter (Systec Controls GmbH), while gas compositions upstream and downstream of the catalyst were determined using Fourier-transform infrared spectroscopy (IAG Versa 06) and an exhaust gas analyser (AVL AMA 4000). The engine was operated under steady-state conditions. The exhaust gas composition at the catalyst inlet and outlet was obtained by alternately sampling two lines connected to the gas analysers. For each measurement point, exhaust gas concentrations were averaged over a 30-second interval to ensure direct comparability between samples. The calculated conversion values therefore represent conversions based on time-averaged inlet and outlet concentrations. Uncertainty in the engine-test conversion values is mainly associated with short-term concentration fluctuations during the averaging interval and the gas-analysis system. Catalyst performance was evaluated by varying the air–fuel equivalence ratio, λ, defined as the ratio of the actual to the stoichiometric air–fuel ratio:

$$\lambda = \frac{(\dot{m}_{air}/\dot{m}_{fuel})}{(\dot{m}_{air}/\dot{m}_{fuel})_{st}} \tag{11}$$

Prior to testing, the catalyst samples were preconditioned for 3 h under fuel-rich (oxygen-deficient) conditions to undergo a standard “de-greening” process. Although this conditioning stage is generally redundant for freshly calcined, laboratory-scale samples, it was intentionally applied here to align with commercial and industrial testing protocols. This procedure ensures a fully stabilised baseline state prior to evaluation, thereby eliminating transient performance variations and removing any trace species remaining from handling or storage that could cause initial active site blocking [31]. Tests were carried out at a fixed engine speed of $1500\,\mathrm{min^{-1}}$ and a load of 150 N m, while λ was varied systematically from 0.9 to 1.4. The detailed engine-test boundary conditions are summarised in Table 1. The engine-test boundary conditions in Table 1 are reported as mean values with standard devia-

Table 1
Engine-test boundary conditions at the investigated air–fuel equivalence ratios. The nominal space time (τ_{nom}) was calculated from the corresponding GHSV values.

λ (-)	T_{inlet} (°C)	T_{outlet} (°C)	Exhaust mass flow rate (kg h^{-1})	GHSV (10^5 h^{-1})	Nominal space time (ms)
0.90	571.5 ± 5.6	519.5 ± 6.1	1.62 ± 0.02	1.41 ± 0.03	25.5 ± 0.6
0.95	583.1 ± 7.3	532.7 ± 3.9	1.60 ± 0.02	1.40 ± 0.03	25.8 ± 0.5
1.00	595.1 ± 7.9	550.6 ± 5.7	1.60 ± 0.03	1.40 ± 0.03	25.7 ± 0.5
1.05	591.2 ± 7.3	522.7 ± 4.3	1.67 ± 0.03	1.41 ± 0.03	25.5 ± 0.5
1.10	577.8 ± 6.6	512.0 ± 3.9	1.71 ± 0.03	1.43 ± 0.02	25.1 ± 0.3
1.40	512.8 ± 1.6	473.1 ± 5.7	2.09 ± 0.02	1.66 ± 0.02	21.7 ± 0.2

tions across the investigated catalyst samples for each λ condition. T_{inlet} and T_{outlet} denote the exhaust-gas temperatures upstream and downstream of the catalyst sample, respectively. The nominal space time, τ_{nom}, was calculated from the GHSV as $\tau_{nom} = 3600/GHSV$, where GHSV is given in h^{-1} and τ_{nom} is obtained in seconds; the values are reported in milliseconds.

Under naturally aspirated operation, a torque of approximately 150 N m was achieved near $\lambda \approx 1.1$, corresponding to a region of high engine thermal efficiency. Variation of λ required coordinated adjustment of both fuel and air mass flow rates in order to maintain the target load. For lean mixtures, the reduced combustion efficiency necessitated an increase in air mass flow, while for rich mixtures the fuel mass flow was increased accordingly. The throttle position was adjusted as required and was fully open only for $\lambda \geq 1.1$. Under leaner conditions, the desired load could not be sustained under naturally aspirated operation; therefore, boosted intake conditions were applied via controlled compressor operation at the engine inlet to maintain the target torque.

Table 2
Geometric characteristics of the selected TPMS unit cells (side length: 10 mm). The volume-specific surface area (s_v) was calculated as the ratio of the geometric surface area to the unit cell volume. Porosity was defined as the ratio of void volume to total unit cell volume (Eq. (4b)). Effective tortuosity was determined as described in Section 2.2.

Cell Type (10 mm)	s_v (mm^{-1})	Porosity (-)	Effective Tortuosity (-)
Schwarz–primitive	0.484	0.9659	1.55
Gyroid	0.635	0.9615	1.60
Edge Position / Flow in x-direction	0.635	0.9615	1.35
Edge Position / Flow in y-direction	0.635	0.9615	1.74
Edge Position / Flow in z-direction	0.635	0.9615	1.70
Schwarz–diamond	0.786	0.9538	1.57
Corner Position / Flow in x-direction	0.758	0.9533	1.54
Corner Position / Flow in y-direction	0.758	0.9533	1.54
Corner Position / Flow in z-direction	0.758	0.9533	1.71

4. Results

4.1. Characterisation of the unit cells

Table 2 shows that the Schwarz–diamond unit cell has the largest volume-specific surface area (0.786 mm^{-1}) while simultaneously displaying the lowest porosity (95.38%) among the three analysed standard configurations. Compared with the gyroid unit cell, the Schwarz–diamond unit cell demonstrates a 23.78% increase in specific surface area, whereas it exhibits a 62.40% increase relative to the Schwarz–primitive unit cell. Despite variations in specific surface area, the porosity values across all three unit cell types remain relatively consistent, with a difference of only 1.21 percentage points between the highest (Schwarz–primitive) and lowest (Schwarz–diamond) porosities for the given unit cell size (10 mm) and wall thickness. As outlined in Section 2.2, the isotropic symmetry of the unit cells is disrupted upon rotation.

4.2. Characterisation of the monoliths

The influence of orientation can be readily understood with reference to columns (a)–(d) in Fig. 3. In its standard orientation, the Schwarz–primitive lattice exhibits the largest apparent frontal flow opening when viewed along the flow direction. Reorienting the structure onto its edge modifies the projected geometry of the flow passages, resulting in a more elongated opening shape. When positioned on its corner, no direct frontal flow opening is visible. A similar trend is observed for the gyroid structure in the edge orientation. For the gyroid structure positioned on its corner, the frontal flow openings appear larger; however, this is accompanied by a reduction in the number of visible openings. In contrast, the Schwarz–diamond lattice exhibits visible frontal flow openings only in the edge orientation, whereas no direct frontal openings are apparent in either the standard or corner-point orientations. The external dimensions of all 27 fabricated monolithic samples were measured after EDM cutting, independent of the internal channel geometry. The samples exhibited a mean height of 50.05 ± 0.05 mm and a mean diameter of 23.86 ± 0.02 mm, showing close agreement with the nominal CAD dimensions of 50 mm height and 23.88 mm diameter and confirming compatibility with the engine-test sample holder. Top views of the investigated TPMS-based and reference monolith geometries are shown in Fig. 8(a). In accordance with previous characterisation of the unit cells and as shown in Table 3, for a given unit-cell size, Schwarz–diamond-based monolithic structures exhibit the largest internal surface area, while Schwarz–primitive-based structures present the smallest. As anticipated, monoliths composed of smaller unit cells present a greater surface area for each TPMS configuration in comparison to those comprising larger unit cells. In comparison to the reference sample featuring hexagonal channels, which possesses an internal surface area of 183 cm^2, five of the eight investigated TPMS structures in Table 3 exhibit higher internal surface areas while maintaining the same total volume of 22.39 cm^3. The exceptions are the 10 mm gyroid-based and Schwarz–primitive-based monoliths. Additionally, it was found that progressively reducing the unit cell size of gyroid structures from a side length of 10 mm to 7.5 mm and further to 5 mm increases the internal surface area from 171.6 cm^2 to 216.3 cm^2 and 304.9 cm^2, respectively. This corresponds to a 26% increase from $GY_{10,s}$ to $GY_{7.5,s}$ and a further 41% increase from $GY_{7.5,s}$ to $GY_{5,s}$, resulting in an overall increase of 78% relative to $GY_{10,s}$. Two gyroid structures in Fig. 2 with linear cell-size gradients along the flow direction, $GY_{G1,s}$ and $GY_{G2,s}$, exhibit surface areas of 207.62 cm^2 and 253.13 cm^2. These values lie between those of the uniformly sized $GY_{10,s}$ and $GY_{5,s}$ configurations, confirming the transitionally graded character of the $GY_{G1,s}$ and $GY_{G2,s}$ structures. In comparison with a monolithic structure with a uniform 7.5 mm unit cell, the graded configuration $GY_{G2,s}$ demonstrates a 17% increase in internal surface area, while $GY_{G1,s}$ attains an internal surface area equivalent to 96% of $GY_{7.5,s}$.

The washcoat loading (Table 3) of the nine samples selected for engine testing from the overall set of 27 washcoated samples ranges from 0.339 to 0.386 g, with a coefficient of variation of approximately

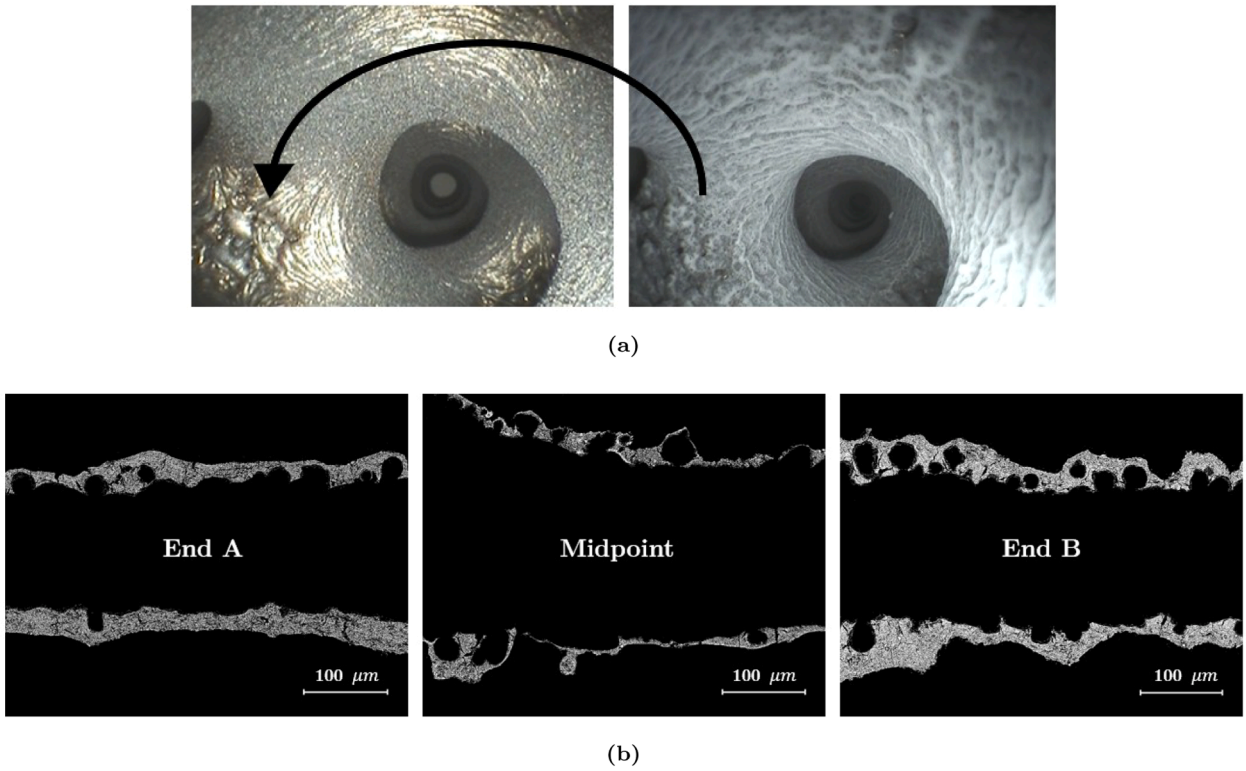

Fig. 5. Axial washcoat thickness distribution along the monolith length. (a) Endoscopic images of the TPMS monolith ($GY_{10,s}$) showing the internal surface appearance before (left) and after (right) washcoating. The arrow highlights a representative surface feature that remains visible after washcoating. (b) Cross-sectional SEM micrographs of the same monolith taken at three axial positions: End A, Midpoint, and End B, illustrating the variation in washcoat thickness along the monolith length.

4.5% (based on a mean loading of 0.365 g and a standard deviation of 0.017 g). For each geometry, the engine-test sample was selected from replicate washcoated samples to minimise differences in washcoat loading across the test set; the individual replicate loadings and corresponding mean and RSD values are provided in Appendix C. In the case of $SD_{5,s}$, this selection was based on samples prepared with the adjusted 10-cycle washcoating procedure, because the initial 12-cycle procedure produced excessive washcoat accumulation for this compact geometry. When normalised by the internal surface area, the corresponding specific loading densities range from 0.9 to 2.4 mg cm^{-2}, with an average value of 1.8 mg cm^{-2}. As expected, lower loading densities are associated with structures possessing larger internal surface areas (e.g. $SD_{5,s}$), whereas higher values are observed for geometries with smaller surface areas (e.g. $SP_{10,s}$). The relative washcoat losses, calculated as $(\Delta m_1 + \Delta m_2)$/Loading, are low for all samples, remaining below 2.5 % in all cases except the edge-positioned Schwarz–diamond structure ($SD_{10,e}$), which exhibits the highest relative loss of 3.7 %. The drop test (Δm_1) assessed washcoat durability against mechanical shock, while the ultrasonic test (Δm_2) served as an accelerated adhesion test to evaluate the resistance of the washcoat to fluid-induced stresses. Overall, these results indicate that the applied washcoating method produced layers with good initial mechanical stability and adhesion across the investigated geometries. The axial coating morphology is illustrated in Fig. 5 using endoscopic and SEM analysis.

Endoscopic inspection confirms homogeneous washcoat coverage along the entire monolith length without macroscopic defects or delamination. Although the surface appears largely homogeneous, localised irregularities are observed. Comparison with the uncoated PBF-LB/M substrate shows that these features originate from intrinsic manufacturing-related surface roughness rather than from coating deficiencies. Cross-sectional SEM images obtained at End A, the midpoint position, and End B demonstrate a non-uniform axial thickness distribution. For most TPMS geometries, the washcoat thickness is higher near both ends and reduced at mid-length. This axial profile is most likely caused by the combined effects of progressive slurry depletion during washcoating and slurry redistribution during spin-drying. Although rotation between successive dipping sequences was applied to minimise directional bias, minor end-to-end differences can still arise from spin-drying-induced redistribution and handling or fixturing effects. In contrast, the reference structure with straight hexagonal channels exhibits a comparatively uniform axial thickness profile without a pronounced mid-length minimum. Because the channel cross-section remains unchanged along the flow direction, slurry infiltration and drainage are expected to occur more uniformly than in the TPMS-based geometries, which may reduce preferential accumulation effects. The micrographs further reveal a porous washcoat structure with interconnected voids and a tortuous internal network. Such a morphology is generally considered beneficial for gas diffusion and reactant accessibility, and may therefore contribute to reduced internal mass-transfer limitations. At the same time, substrate-induced surface texture and partially fused powder features introduce local variations in washcoat morphology, as exemplified by the surface feature highlighted in Fig. 5(a). This interplay reflects a trade-off between washcoat uniformity and mechanical interlocking: the rough PBF-LB/M surface promotes strong adhesion of the ceramic γ-Al_2O_3 washcoat, consistent with the low relative coating losses reported in Table 3, while introducing local variations in washcoat thickness and surface morphology. The investigated specimens exhibited comparable total washcoat loadings, suggesting that differences in catalytic performance can be primarily attributed to geometric effects rather than variations in catalyst mass. EDS point analyses of the washcoat in the investigated $GY_{5,s}$ sample yielded an average Pt content close to the nominal loading of 2 wt% (Appendix B), indicating no substantial Pt loss at the analysed locations during catalyst preparation and washcoat deposition.

Table 3
Characteristics of the TPMS-based monoliths. Surface area, geometric specific surface area, and porosity correspond to the uncoated 50 mm monolith geometries. Washcoat thickness, washcoat loading, and mass-loss values refer to the corresponding washcoated samples.

Sample	Surface Area	s_v	Porosity	Washcoat Thickness (μm)			Loading	Δm_1	Δm_2
	(cm^2)	(mm^{-1})	(-)	End A	Midpoint	End B	(g)	(g)	(g)
$GY_{10,s}$	171.61	0.77	0.961	25.4 ± 10.1	16.0 ± 14.0	29.0 ± 14.4	0.370	0.0002	0.0012
$GY_{5,s}$	304.88	1.36	0.923	33.0 ± 12.4	19.0 ± 10.1	25.1 ± 11.0	0.386	0.0015	0.0011
$GY_{10,c}$	176.92	0.79	0.960	42.0 ± 7.9	15.4 ± 4.4	33.7 ± 14.2	0.383	0.0006	0.0020
$SD_{10,s}$	201.78	0.90	0.954	27.7 ± 13.1	13.3 ± 4.0	34.2 ± 11.2	0.357	0.0032	0.0037
$SD_{5,s}$	369.88	1.65	0.907	34.3 ± 10.1	–	33.0 ± 11.3	0.344	0.0031	0.0047
$SD_{10,e}$	204.49	0.91	0.953	32.7 ± 10.6	14.5 ± 9.0	24.0 ± 8.7	0.377	0.0052	0.0089
$SP_{10,s}$	139.07	0.62	0.931	32.7 ± 12.4	10.8 ± 4.7	28.6 ± 10.3	0.339	0.0012	0.0001
$SP_{5,s}$	235.33	1.05	0.864	28.1 ± 10.5	15.4 ± 7.8	33.7 ± 18.1	0.372	0.0011	0.0019
REF	183.00	0.82	0.354	28.1 ± 10.0	21.9 ± 9.9	31.7 ± 7.4	0.361	0.0007	0.0030

4.3. Pressure drop

Based on their combined geometric characteristics, including effective tortuosity (in Table 2), flow-passage dimensions, and frontal accessibility, Schwarz–primitive-based monoliths were anticipated to exhibit lower pressure drops than Schwarz–diamond-based monoliths. Moreover, a reduction in unit cell size increases the specific surface area (s_v) and decreases the characteristic flow-passage dimensions, which together are expected to result in higher pressure drops. All measurements were conducted using uncoated monolithic substrates; therefore, the observed pressure drop reflects geometric effects of the channel architecture without influence from a catalytic washcoat. Accordingly, the pressure-drop data are used here as a comparative hydrodynamic screening of the investigated topologies rather than as a direct pressure-drop measurement under the exact coated engine-test configuration. The measured pressure drop values shown in Fig. 6 are consistent with these expectations. When expressed as pressure drop per unit length as a function of the specific surface area (s_v), the TPMS geometries show a general increase in pressure drop with increasing s_v, although the relationship is not purely monotonic. The apparent near-linear alignment of several data points should therefore be understood as an empirical trend within the present geometry set, rather than as a generally valid theoretical scaling law. The reference monolith is included as a benchmark, and the dashed grey horizontal and vertical lines indicate its pressure drop per unit length and specific surface area, respectively. The $SD_{5,s}$ monolith exhibits the highest pressure drop per unit length, whereas the $SP_{10,s}$ configuration shows the lowest value, even below that of the reference (REF) monolith with straight channels. Consistent with this trend, Schwarz–primitive-based monoliths generally exhibit lower pressure drops than Schwarz–diamond-based structures. At the same time, geometries with similar s_v values show noticeable differences in pressure drop, indicating that additional geometric characteristics influence the flow behaviour. This is also evident from the comparison with the reference monolith: although the reference has a specific surface area comparable to several of the 10 mm TPMS structures, noticeable differences in pressure drop per unit length are observed, further indicating the influence of topology-dependent geometric characteristics. In particular, variations in unit cell morphology are associated with differences in geometric tortuosity, channel connectivity, and flow-path uniformity. Overall, the results show that the specific surface area (s_v) is an important geometric parameter influencing pressure drop, while differences between geometries indicate the additional influence of unit cell topology, i.e. the connectivity and arrangement of the flow paths within the unit cell.

4.4. Catalytic performance under engine exhaust conditions

Using the $GY_{10,s}$ structure as a representative example, pollutant concentrations measured at the catalyst inlet and outlet are shown in Fig. 7 as a function of the air–fuel equivalence ratio (λ). The observed trends in CH_4, CO, and NO_x emissions are consistent with typical internal combustion engine behaviour and confirm that the engine provides a realistic and reproducible exhaust environment for catalyst evaluation. Outlet concentrations are included to enable direct assessment of catalytic conversion. CO concentrations decrease markedly from rich to stoichiometric conditions, with outlet concentrations remaining very low under stoichiometric and lean conditions. CH_4 concentrations decrease towards $\lambda \approx 1$, where the lowest outlet values are observed. This behaviour is attributed to the coupled change in exhaust-gas boundary conditions during engine operation. Under simplified conditions with constant temperature, residence time, and gas composition, increasing λ would be expected to promote CH_4 oxidation because of the higher oxygen availability. In the present engine-bench experiments, however, increasing λ above stoichiometric conditions decreased the exhaust-gas temperature and increased the exhaust mass flow rate and GHSV, resulting in a shorter nominal space time (Table 1). Since CH_4 oxidation over Pt/γ-Al_2O_3 is strongly temperature-dependent, the lower temperature and shorter residence time under lean operation can outweigh the beneficial effect of increased oxygen availability. The lowest CH_4 outlet concentration near $\lambda = 1$ is therefore attributed to the combination of sufficient oxygen availability, maximum exhaust-gas temperature, and favourable residence time under stoichiometric operation. Similarly, NO_x outlet concentrations remain comparatively low under rich-to-stoichiometric conditions and increase sharply under lean operation, while NO_x conversion reaches its highest value near $\lambda = 1$. Since all converters were coated with platinum and exhibited comparable coating stability and loading reproducibility (see Section 4.2), the experiments focus on the catalytic performance of the additively manufactured structures. The pollutant conversion, X_i, is defined as the relative reduction in species concentration between the catalyst inlet and outlet:

$$\mathbf{X_i} = \frac{\mathbf{c_{i,in}} - \mathbf{c_{i,out}}}{\mathbf{c_{i,in}}} \times 100\ \% \tag{12}$$

The subscript i in Eq. (12) denotes CO, CH_4, or NO_x. The conversion is evaluated based on measured concentrations, assuming negligible changes in gas density and volumetric flow rate across the catalyst.

Fig. 8 illustrates the investigated monolith geometries and the relationship between washcoat-loading-normalised CO conversion and geometric specific surface area (s_v) under stoichiometric conditions ($\lambda = 1$). The top-view images in Fig. 8(a) show the different frontal openings and channel morphologies of the washcoated TPMS-based monoliths and the straight-channel reference monolith, while Fig. 8(b) compares their catalytic performance after normalisation by the corresponding washcoat loading. Among the investigated TPMS geometries, higher s_v is broadly associated with higher washcoat-loading-normalised CO conversion, although the relationship is clearly non-monotonic. This suggests that geometric surface area contributes to catalyst utilisation but does not alone determine catalytic performance. However, geometries with comparable s_v exhibit noticeable differences in washcoat-loading-normalised conversion. Because the conversion values are normalised

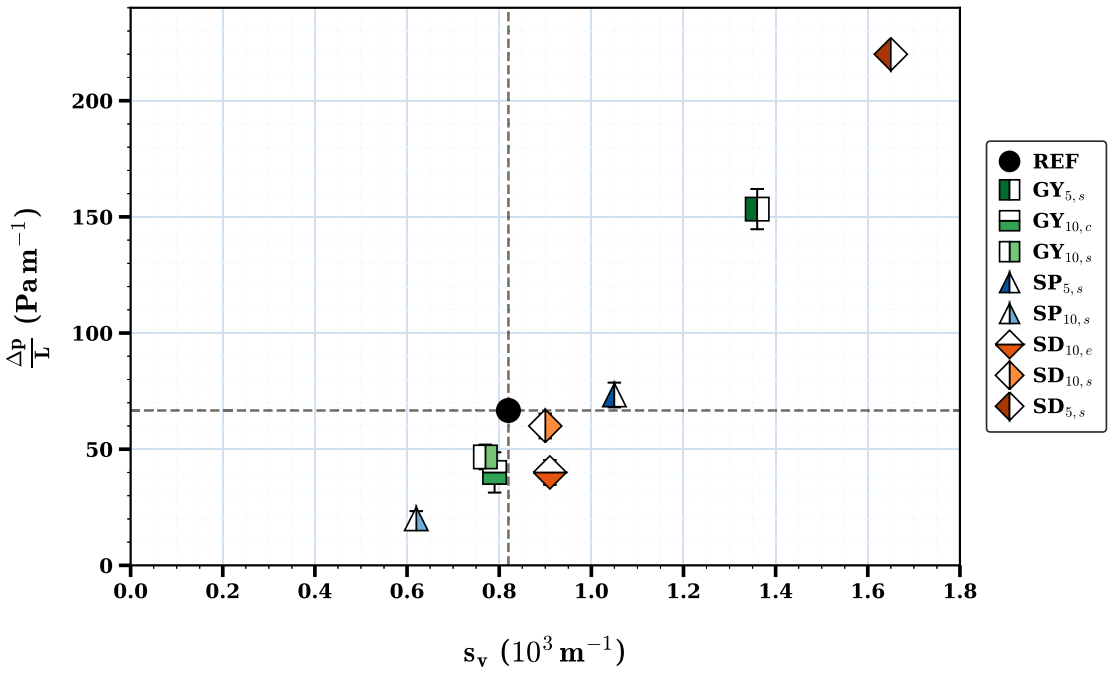

Fig. 6. Pressure drop per unit length as a function of geometric specific surface area (s_v) for the investigated monolith geometries. Error bars indicate standard deviations from three repeated pressure-drop measurements ($n = 3$) performed on the same specimen for each geometry, and dashed lines mark the corresponding REF values for s_v and $\Delta p/L$.

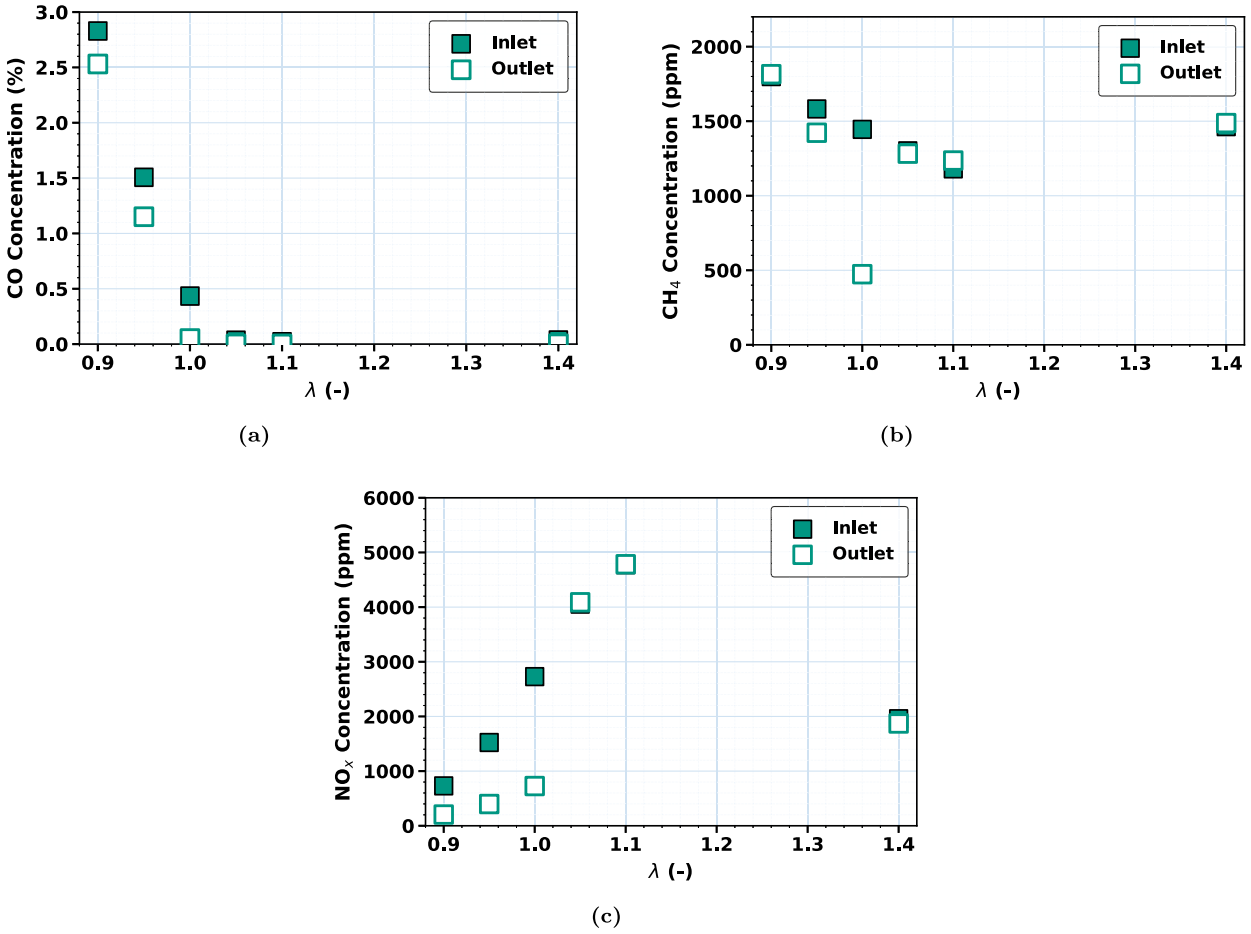

Fig. 7. Pollutant concentrations at the catalyst inlet and outlet as a function of the air–fuel equivalence ratio for the $GY_{10,s}$ structure. Filled symbols denote inlet concentrations, while open symbols represent outlet concentrations.

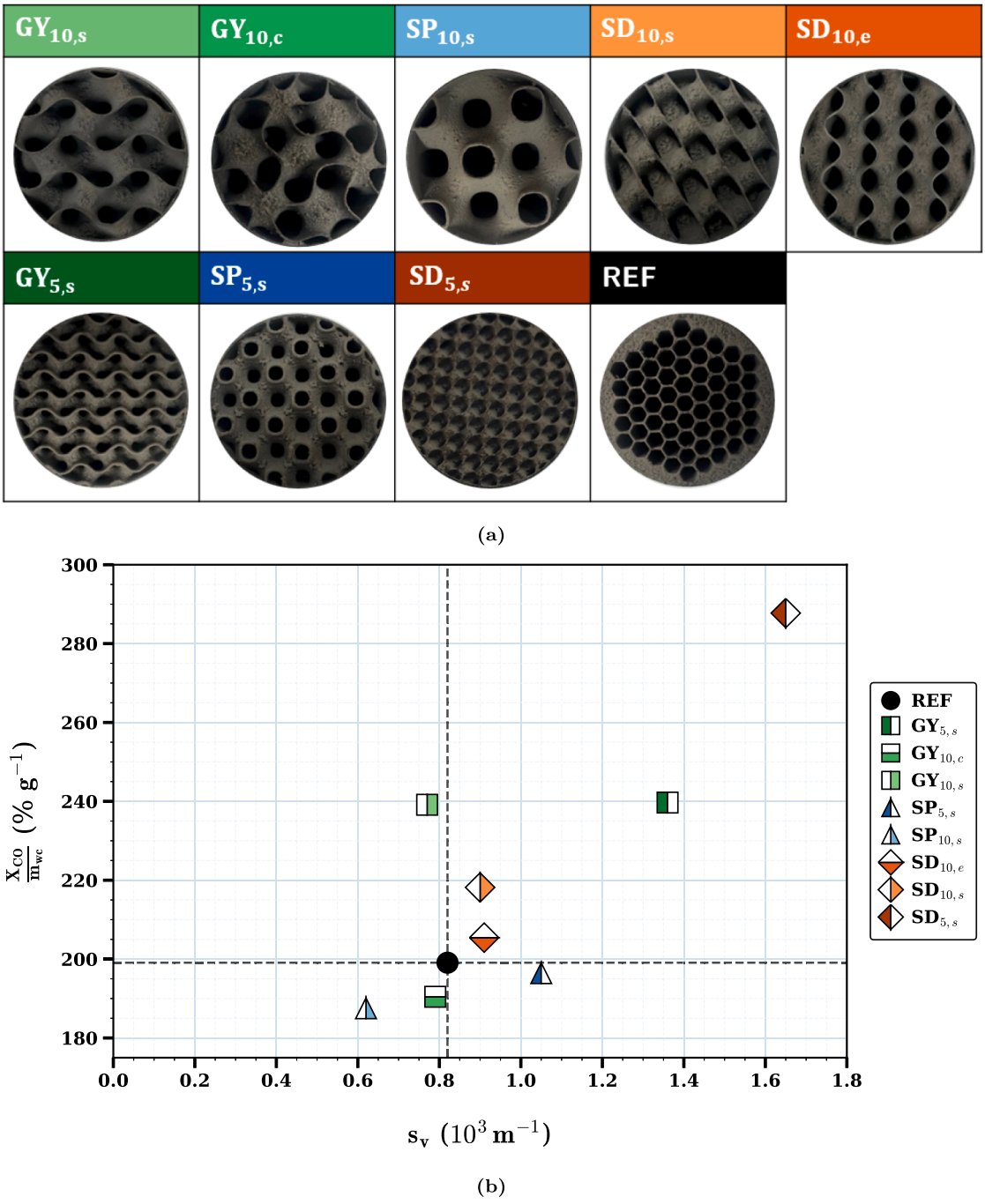

Fig. 8. Monolith geometries and washcoat-loading-normalised CO conversion. (a) Top views of the washcoated TPMS-based monoliths and the straight-channel reference monolith (REF). (b) CO conversion normalised by washcoat loading (m_{wc}) as a function of geometric specific surface area (s_v). Dashed grey lines indicate the REF values.

by washcoat loading, the comparison emphasises differences in catalyst utilisation rather than differences caused primarily by the amount of deposited washcoat. The remaining variations therefore point to the influence of geometry-dependent factors such as flow distribution, accessibility of the washcoated catalytic surface, and mass transport within the structure.

For the gyroid-based structures, the samples $GY_{10,s}$ and $GY_{10,c}$ exhibit clearly different washcoat-loading-normalised conversion values despite comparable s_v, indicating a pronounced influence of unit cell orientation. In contrast, the Schwarz–diamond geometries $SD_{10,s}$ and $SD_{10,e}$ show more comparable washcoat-loading-normalised conversion values at comparable s_v, indicating a weaker sensitivity to orientation within the tested configurations. This may be related to the comparatively restricted frontal openings of the Schwarz–diamond structures, which could limit orientation-induced changes in flow accessibility.

Furthermore, a reduction in unit cell size from 10 mm to 5 mm leads to an increase in s_v and, consequently, higher washcoat-loading-normalised conversion for the Schwarz–diamond geometry, while the corresponding changes are less pronounced for the gyroid and Schwarz–primitive topology families. This effect is most pronounced for the Schwarz–diamond structures, where $SD_{5,s}$ exhibits the highest washcoat-loading-normalised conversion among all investigated samples. For the Schwarz–primitive structures, $SP_{5,s}$ shows a slightly higher washcoat-loading-normalised conversion than $SP_{10,s}$, consistent with its

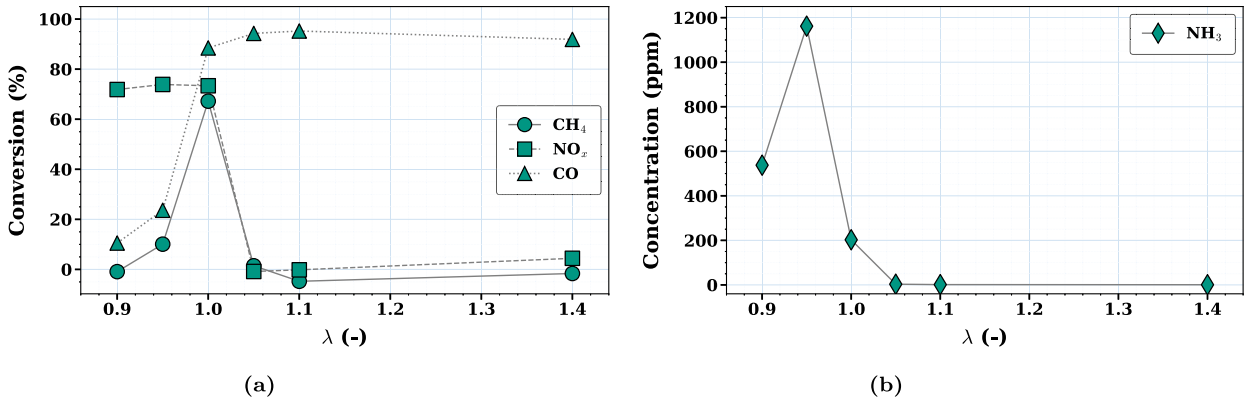

Fig. 9. Catalytic conversion over the additively manufactured TPMS-based converter $GY_{10,s}$. Panel (a) displays the conversions of CH_4, CO, and NO_x, while panel (b) shows the NH_3 concentration. Lines connecting the data points are included solely as visual guides and do not represent fitted trend lines.

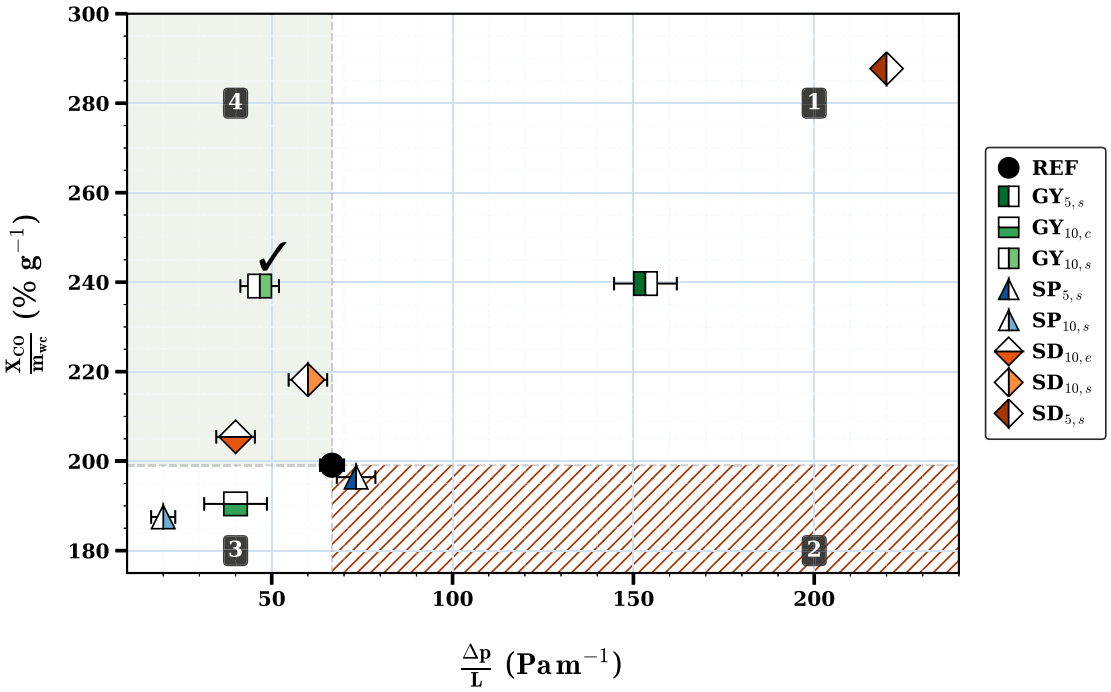

Fig. 10. Performance map of washcoat-loading-normalised CO conversion. CO conversion normalised by washcoat loading (m_{wc}) is plotted as a function of pressure drop per unit length ($\Delta p/L$). Dashed grey lines indicate the REF values and determine the four performance regions. The check mark identifies $GY_{10,s}$, which provides one of the most favourable conversion–pressure-drop balances among the investigated configurations. Horizontal error bars indicate standard deviations from three repeated pressure-drop measurements ($n = 3$) performed on the same specimen for each geometry.

higher s_v. However, both SP configurations remain below the reference monolith; therefore, this difference is interpreted only as a qualitative intra-topology trend and not as a statistically significant performance improvement.

The reference sample (REF) exhibits a washcoat-loading-normalised conversion comparable to several TPMS-based geometries, despite differences in topology and specific surface area. This indicates that a higher specific surface area alone does not guarantee superior catalyst utilisation. However, the highest washcoat-loading-normalised performance is achieved by $SD_{5,s}$, followed by high-performing gyroid-based structures such as $GY_{5,s}$ and $GY_{10,s}$. Considering the corresponding non-normalised CO conversion values at $\lambda = 1$, the two highest-conversion TPMS configurations exceeded 90% CO conversion, with $SD_{5,s}$ reaching the highest value of approximately 99%. Within the proof-of-concept scope of this study, the geometry-dependent catalytic results are therefore interpreted as comparative performance trends, while broader statistical validation across replicate engine-tested samples remains a subject for future work.

To further elucidate the catalytic behaviour, the $GY_{10,s}$ monolith is examined in more detail. While the preceding discussion focused on geometry-dependent CO conversion, the following analysis addresses the broader catalytic behaviour of the platinum-washcoated monolith. As shown in Fig. 9, the conversions of CH_4 and NO_x reach their highest values near stoichiometric conditions ($\lambda \approx 1$), consistent with the exhaust-gas temperature, GHSV, and nominal space-time trends reported in Table 1. This behaviour indicates partial three-way catalytic (TWC) functionality in addition to efficient CO oxidation. Minor negative conversion values observed for CH_4 and NO_x under lean operating conditions indicate slightly higher outlet than inlet concentrations. Given the small magnitude of these deviations relative to the corresponding inlet concentrations, they may be within the experimental uncertainty of the gas-analysis measurements. Under rich operating con-

ditions ($\lambda < 1$), NH_3 formation is observed, with peak concentrations occurring where NO_x conversion remains substantial, while CH_4 conversion is comparatively low. This behaviour is characteristic of NO_x reduction to NH_3 over platinum-group metals under reducing conditions, where CO and H_2 act as the primary reductants [32]. The presence of NH_3 should therefore be interpreted as in-situ formation from NO_x reduction on the catalyst surface, rather than NH_3 slip, since no external ammonia is introduced into the system. These results demonstrate that the catalyst facilitates not only oxidation reactions but also reductive NO_x conversion pathways, confirming extended three-way catalytic functionality of the additively manufactured converter. The alumina washcoat provides a high-surface-area support for platinum dispersion, enabling the observed reactivity, while the stainless steel carrier primarily ensures thermal and mechanical stability under engine-relevant conditions. Together, this architecture supports the multifunctional catalytic behaviour observed across rich, stoichiometric, and lean operating regimes.

5. Discussion

The combined performance map presented in Fig. 10 summarises the trade-off between washcoat-loading-normalised CO conversion and pressure drop per unit length for the investigated TPMS-based monoliths relative to the straight-channel reference monolith (REF). The pressure-drop data were obtained from uncoated 150 mm-long substrates, whereas catalytic performance was evaluated using washcoated samples under real CNG engine exhaust conditions. Therefore, the map should be interpreted as a topology-screening guide rather than as a direct one-to-one operating validation. Nevertheless, it provides useful insight into how geometric design parameters influence the balance between catalyst utilisation and hydrodynamic resistance. The straight-channel reference monolith provides a controlled geometric benchmark because it was manufactured, washcoated, calcined, and tested under the same conditions as the TPMS-based samples. However, it should not be interpreted as a direct substitute for a commercial automotive catalyst substrate, for which cell density, wall thickness, catalyst formulation, thermal mass, ageing state, and operating conditions may differ. Direct benchmarking against application-relevant commercial substrates under matched conditions therefore remains necessary. In this performance map, the four regions should be interpreted as continuous performance domains rather than as a point-by-point classification. Region 4 represents the most favourable domain, where higher washcoat-loading-normalised CO conversion is combined with lower pressure drop per unit length relative to REF. This behaviour is observed for $GY_{10,s}$ and the 10 mm Schwarz–diamond configurations, indicating that favourable catalyst utilisation can be achieved without a pressure-drop penalty when the flow passages remain sufficiently accessible. In contrast, Region 1 contains compact high-s_v structures, most notably $SD_{5,s}$ and $GY_{5,s}$, for which the high washcoat-loading-normalised conversion is accompanied by a pronounced increase in pressure drop. Region 3 represents the opposite trade-off, where more open geometries reduce hydrodynamic resistance but also provide lower catalyst utilisation than REF. Region 2 corresponds to the least favourable domain, where lower washcoat-loading-normalised conversion is accompanied by higher pressure drop per unit length than REF. Samples located in or close to this region indicate that an unfavourable combination of topology, orientation, and flow accessibility can reduce catalyst utilisation while increasing flow resistance. The results show that the performance of the investigated TPMS carriers cannot be described by specific surface area (s_v) alone. Although a higher s_v increases the available geometric area for catalyst deposition and gas–surface contact, samples with comparable s_v values exhibit different pressure-drop and washcoat-loading-normalised conversion behaviour. This indicates that additional topology-dependent parameters, including channel connectivity, effective tortuosity, frontal flow accessibility, and flow-path uniformity, also influence catalyst accessibility and mass transport within the monolith.

The compact 5 mm unit cell structures, particularly $SD_{5,s}$ and $GY_{5,s}$, illustrate both the benefit and the penalty of increasing geometric compactness. The need to reduce the number of washcoating cycles for $SD_{5,s}$ further suggests that this compact Schwarz–diamond geometry can retain slurry more strongly than the more open structures, consistent with its high surface area and reduced characteristic flow-passage dimensions. Their high specific surface areas provide a larger catalyst-coated interface for gas–surface contact, which is consistent with their high washcoat-loading-normalised CO conversion. The particularly high washcoat-loading-normalised CO conversion of $SD_{5,s}$ is consistent with its combination of the highest s_v in the investigated set, restricted flow-passage dimensions, and the Schwarz–diamond channel network; together, these features likely increase gas–wall interaction and utilisation of the washcoated catalytic surface. At the same time, the smaller flow passages and more tortuous internal channel networks increase wall interaction and flow resistance, resulting in higher pressure drops. This behaviour reflects the expected trade-off between improved catalyst accessibility and increased hydrodynamic resistance when the characteristic flow-passage dimensions are reduced. In contrast, the Schwarz–primitive configurations represent a more open geometric limit. The $SP_{10,s}$ structure exhibits the lowest pressure drop per unit length, even below that of REF, but its washcoat-loading-normalised CO conversion remains lower than the reference value. This suggests that its open and less tortuous flow paths reduce resistance but provide insufficient gas–surface interaction for high catalyst utilisation. The $SP_{5,s}$ structure shows a slightly higher washcoat-loading-normalised CO conversion than $SP_{10,s}$, consistent with its higher s_v, but this is accompanied by a higher pressure drop. Since both SP configurations remain below REF in washcoat-loading-normalised CO conversion and only one engine-test sample per geometry was evaluated, this difference is interpreted only as a qualitative intra-topology trend rather than as a statistically significant performance improvement. The gyroid configuration $GY_{10,s}$ provides one of the most favourable overall balances between conversion and pressure drop. Its intermediate specific surface area, continuous channel connectivity, and accessible flow passages appear to provide sufficient gas–surface interaction while avoiding the pronounced pressure-drop penalty observed for the compact 5 mm structures. This explains why $GY_{10,s}$ lies in the favourable region of Fig. 10, combining higher washcoat-loading-normalised CO conversion with lower pressure drop per unit length relative to REF. The difference between $GY_{10,s}$ and $GY_{10,c}$ further highlights the importance of unit cell orientation, since both structures have comparable specific surface areas but differ markedly in their conversion–pressure-drop behaviour. Normalisation by washcoat loading further supports the interpretation that the observed performance differences are not governed only by the amount of deposited washcoat. Instead, the results suggest that the spatial accessibility of the washcoated surface, controlled by the TPMS geometry, plays an important role in determining catalyst utilisation. The rough PBF-LB/M surface and porous washcoat morphology can promote mechanical interlocking and reactant accessibility, while local variations in washcoat thickness and flow distribution may further influence local mass transport. The low relative washcoat losses measured after the drop and ultrasonic tests support the good initial mechanical stability of the deposited layers across the investigated geometries. However, these tests represent accelerated adhesion screening rather than validation of durability over extended engine operation. Under practical service conditions, thermal cycling and vibration may generate interfacial stresses, crack propagation, or local delamination, while prolonged high-temperature exposure may contribute to washcoat sintering and catalyst deactivation [4,11]. Therefore, the present adhesion results establish a favourable initial condition, while application-level durability validation requires prolonged engine operation, thermal ageing, vibration testing, and post-test assessment of washcoat integrity and catalytic activity. Overall, the experimental results indicate that the conversion–pressure-drop behaviour of additively manufactured TPMS catalyst carriers is controlled by the interplay between specific surface area, unit

cell topology, effective tortuosity, flow distribution, and catalyst accessibility. The present study therefore demonstrates that TPMS architectures provide a tunable design platform for balancing catalytic performance and hydrodynamic resistance. A fully resolved mechanistic separation of the effects of topology, residence-time distribution, local velocity fields, and mass-transfer effects will require dedicated CFD-based analysis, which is identified as an important next step.

6. Conclusion and outlook

6.1. Conclusion

This study successfully exploited the design freedom offered by laser powder bed fusion (PBF-LB/M) to manufacture stainless-steel TPMS catalyst carriers and systematically evaluate their manufacturability, coating compatibility, hydrodynamic behaviour, and catalytic performance. The results demonstrate that the catalytic behaviour of the investigated TPMS-based monoliths is not governed by geometric specific surface area (s_v) alone. Although higher s_v generally increases the available catalyst-coated interface for gas–surface interaction, the comparison of geometries with similar s_v shows that unit cell topology, orientation, flow accessibility, and effective tortuosity also strongly affect catalyst utilisation. These topology-dependent fluid-dynamic and mass-transport characteristics influence both the washcoat-loading-normalised CO conversion and the overall pollutant-conversion behaviour. The combined performance analysis based on washcoat-loading-normalised CO conversion and pressure drop per unit length further shows that the investigated TPMS structures occupy different conversion–pressure-drop domains relative to the straight-channel reference monolith. Compact high-s_v structures such as $SD_{5,s}$ and $GY_{5,s}$ provide high washcoat-loading-normalised conversion, but this benefit is accompanied by increased pressure drop. In contrast, more open structures such as $SP_{10,s}$ reduce hydrodynamic resistance but show lower catalyst utilisation. Among the investigated configurations, $GY_{10,s}$ provides one of the most favourable overall balances and lies within Region 4, combining higher washcoat-loading-normalised CO conversion with lower pressure drop per unit length than the reference monolith. The study also demonstrates that complex TPMS geometries can be fabricated by PBF-LB/M as metallic catalyst-carrier architectures suitable for subsequent washcoating. Good initial washcoat adhesion was demonstrated in the applied adhesion tests, together with catalytic activity under real CNG engine exhaust conditions, supporting the potential of these structures for catalytic applications. Overall, the findings demonstrate that additively manufactured TPMS catalyst carriers offer a promising route towards tailoring the balance between catalytic performance and hydrodynamic resistance. The results further establish a framework for the digital design of application-specific catalyst supports and highlight the potential of TPMS architectures for broader catalytic and thermal engineering applications.

6.2. Outlook

The present study establishes the experimental feasibility of PBF-LB/M-manufactured, washcoated TPMS catalyst carriers under real engine exhaust conditions and identifies promising topology-dependent performance trends. Future work should also focus on numerical simulations of pressure drop and mass transport for such TPMS geometries. This will enable a more detailed analysis of local flow fields, species transport, residence-time distributions, and catalyst accessibility, thereby providing mechanistic insight into the experimentally observed differences in catalytic conversion and pressure drop. Such CFD-based analysis would help to distinguish the relative contributions of specific surface area, tortuosity, flow distribution, and mass-transfer effects. Complementary X-ray computed tomography could further quantify internal wall-thickness distribution, local porosity, and surface-area fidelity of the printed TPMS geometries, thereby providing additional geometric input for future structure–performance analysis. Further studies may also advance the present proof-of-concept towards application-oriented validation through long-term durability and vibration-resistance testing, thermal ageing, assessment of catalyst deactivation, benchmarking against application-relevant commercial catalyst substrates under comparable operating conditions, scale-up and manufacturing-feasibility assessment, and techno-economic evaluation.

CRediT authorship contribution statement

Fatemeh Mehdipour: Writing – review & editing, Writing – original draft, Visualization, Validation, Software, Methodology, Investigation, Formal analysis, Data curation, Conceptualization; **Jan Erik Heinrich:** Writing – review & editing, Investigation, Data curation; **Zexin Yu:** Writing – review & editing, Investigation, Data curation; **Martin Kutscherauer:** Writing – review & editing, Validation; **Michael Robert Tucker:** Writing – review & editing; **Michael Rubin:** Writing – review & editing, Validation, Supervision; **Uwe Wagner:** Writing – review & editing, Validation, Supervision, Resources; **Thomas Koch:** Writing – review & editing, Supervision, Resources, Project administration, Funding acquisition; **Roland Dittmeyer:** Writing – review & editing, Supervision, Project administration, Funding acquisition.

Declaration of generative AI and AI-assisted technologies in the manuscript preparation process

During the preparation of this work the authors used ChatGPT in order to improve the readability and the language of the manuscript. After using this tool, the authors reviewed and edited the content as needed and take full responsibility for the content of the published article.

Declaration of competing interest

The authors declare that they have no known competing financial interests or personal relationships that could have appeared to influence the work reported in this paper.

Acknowledgements

The authors gratefully acknowledge Prof. Dr.-Ing. Christoph Klahn for valuable discussions and input on the scientific relevance of this work. The authors also thank Uta Gerhards and Florian Messerschmidt for performing the SEM and WDX measurements, and Manuel Hofheinz for his support with the manufacturing and post-processing of the PBF-LB/M test designs. This work was funded by the Deutsche Forschungsgemeinschaft (DFG, German Research Foundation) – Project-ID 426888090 – SFB 1441.

Data availability

Data will be made available on request.

Appendix A. Engine test setup

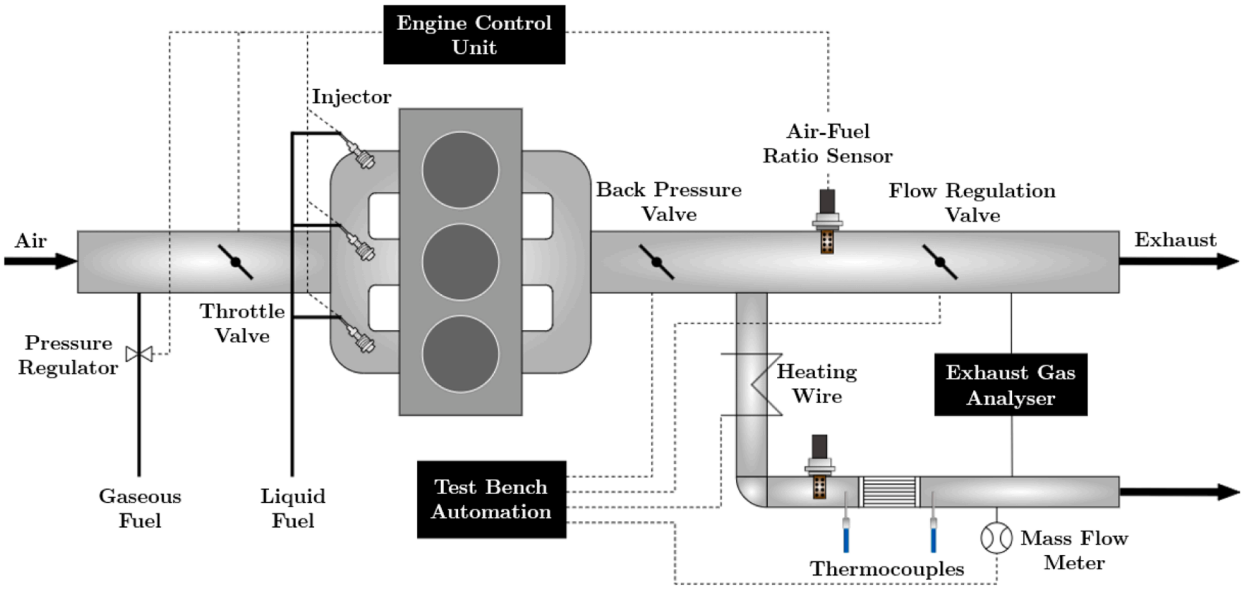

Fig. A.1. Engine test setup for catalytic performance evaluation. Exhaust gas was directed through a bypass line containing the catalytic sample. Flow rate, temperature, and gas composition were monitored using a mass flow meter, thermocouples, and exhaust gas analysers.

Appendix B. WDX analysis

Wavelength-dispersive X-ray spectroscopy (WDX) analysis of the washcoated $GY_{5,s}$ structure is shown in Fig. B.1. The elemental maps illustrate the spatial distribution of O, Al, Pt, and Fe across the washcoat/carrier interface. To complement the WDX mapping results, energy-dispersive X-ray spectroscopy (EDS) point analyses were performed at three different locations within the washcoat layer. The average elemental composition obtained from these measurements is summarised in Table B.1.

Table B.1
Average elemental composition of the washcoat layer for sample $GY_{5,s}$ obtained from three EDS point analyses.

	O (mass%)	Al (mass%)	Pt (mass%)
Average	46.51	51.24	2.13

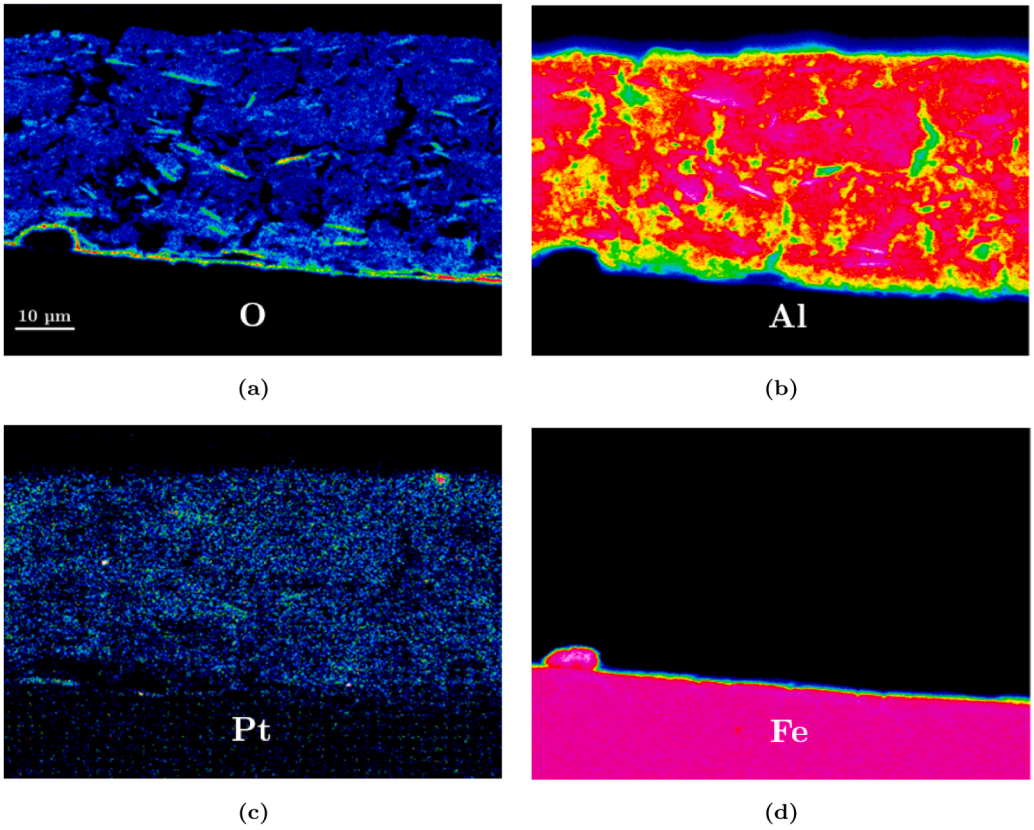

Fig. B.1. WDX elemental maps of the washcoated $GY_{5,s}$ structure showing the spatial distribution of O, Al, Pt, and Fe across the washcoat/substrate interface.

Appendix C. Replicate washcoat loadings

For each investigated geometry, replicate samples were washcoated, and one sample was selected for engine testing to minimise differences in final washcoat loading across the engine-test set. The selected value is shown in **bold** in Table C.1.

Table C.1
Replicate washcoat loadings used for statistical evaluation.

Sample	Replicate loadings (g)	Mean loading ± SD (g)	RSD (%)
$GY_{10,s}$	0.424, 0.327, **0.370**	0.374 ± 0.048	13.0
$GY_{5,s}$	0.450, 0.384, **0.386**	0.407 ± 0.038	9.2
$GY_{10,c}$	0.440, 0.342, **0.383**	0.388 ± 0.049	12.7
$SD_{10,s}$	0.435, **0.357**, 0.390	0.394 ± 0.039	9.9
$SD_{5,s}$	0.360[a], **0.344**[a]	0.352 ± 0.011	3.2
$SD_{10,e}$	0.430, **0.377**, 0.411	0.406 ± 0.027	6.6
$SP_{10,s}$	**0.339**, 0.299, 0.320	0.319 ± 0.020	6.3
$SP_{5,s}$	**0.372**, 0.352, 0.385	0.370 ± 0.017	4.5
REF	0.394, 0.455, **0.361**	0.403 ± 0.048	11.8

Mean loading, standard deviation (SD), and relative standard deviation (RSD) were calculated from the replicate values listed in Table C.1. For $SD_{5,s}$, values marked with superscript[a] were obtained using the adjusted 10-cycle washcoating procedure and were used for the statistical evaluation. The initial 12-cycle washcoating of $SD_{5,s}$ resulted in a substantially higher loading of 0.518 g, revealing excessive washcoat accumulation for this geometry under the standard washcoating procedure. This value was therefore not included in the statistical evaluation.

Appendix D. Explanation of concentration units for exhaust gas species

Typical concentration ranges and corresponding units are summarised in Table D.1. These conventions align with standard emission measurement practices and established literature [31,33].

Table D.1
Exhaust gas concentrations and reporting units.

Gas	Typical Range	Reported Unit	Rationale
CO	0.1–3 %	vol%	Major product of incomplete combustion
CH_4	100–2000	ppm	Unburned hydrocarbon (minor species)
NO_x	100–5000	ppm	Regulated emission component

References

[1] I.D. Williams, M. Blyth, Autogeddon or autoheaven: environmental and social effects of the automotive industry from launch to present, Sci. Total Environ. 858 (2023) 159987.

[2] E. Kritsanaviparkporn, F.M. Baena-Moreno, T.R. Reina, Catalytic converters for vehicle exhaust: fundamental aspects and technology overview for newcomers to the field, Chemistry 3 (2) (2021) 630–646.

[3] M. Kozioł-Jarosz, M. Brzeżański, The role and tasks of the support mats in the construction of catalytic converters, Combust. Engines 170 (3) (2017) 96–99. https://doi.org/10.19206/CE-2017-315

[4] D. Wu, H. Zhang, Mechanical stability of monolithic catalysts: scattering of washcoat adhesion and failure mechanism of active material, Ind. Eng. Chem. Res. 52 (41) (2013) 14713–14721.

[5] P. Liu, G.-F. Chen, Porous Materials: Processing and Applications, Elsevier, 2014.

[6] P. Avila, M. Montes, E.E. Miró, Monolithic reactors for environmental applications: a review on preparation technologies, Chem. Eng. J. 109 (1-3) (2005) 11–36.

[7] A. Cybulski, J.A. Moulijn, Monoliths in heterogeneous catalysis, Catalysis Rev.–Sci. Eng. 36 (2) (1994) 179–270.

[8] F.-J. Hanel, E. Otto, R. Brück, Electrically heated catalytic converter (EHC) in the BMW ALPINA B12 5.7 switch-Tronic, SAE Trans. 105 (1996) 228–236.

[9] K. Li, B. Xiao, Y. Wang, J. Jia, X. Wu, Applications of electric heating technology in vehicle exhaust pollution control, Processes 12 (2) (2024) 298.

[10] M. Nonnenmann, Metal supports for exhaust gas catalysts, SAE Trans. 94 (1985) 814–821.

[11] A. Montebelli, C.G. Visconti, G. Groppi, E. Tronconi, C. Cristiani, C. Ferreira, S. Kohler, Methods for the catalytic activation of metallic structured substrates, Catal. Sci. Technol. 4 (9) (2014) 2846–2870.

[12] A.M. Holmgren, Enhanced mass transfer in monolith catalysts with bumps on the channel walls, Ind. Eng. Chem. Res. 38 (5) (1999) 2091–2097.

[13] G.L. Vaneman, Comparison of metal foil and ceramic monolith automotive catalytic converters, in: Studies in Surface Science and Catalysis, Vol. 71, Elsevier, 1991, pp. 537–545.

[14] H. Santos, M. Costa, Evaluation of the conversion efficiency of ceramic and metallic three way catalytic converters, Energy Convers. Manag. 49 (2) (2008) 291–300.

[15] F. Mehdipour, T. Delrieux, F. Maurer, J.-D. Grunwaldt, C. Klahn, R. Dittmeyer, Opportunities and limitations of metal additive manufacturing of structured catalytic converters, Catal. Commun. 187 (2024) 106873.

[16] O.A. Alimi, C.A. Akinnawo, R. Meijboom, Monolith catalyst design via 3D printing: a reusable support for modern palladium-catalyzed cross-coupling reactions, New J. Chem. 44 (43) (2020) 18867–18878.

[17] G.J.H. Lim, Y. Wu, B.B. Shah, J.J. Koh, C.K. Liu, D. Zhao, A.K. Cheetham, J. Wang, J. Ding, 3D-printing of pure metal–organic framework monoliths, ACS Mater. Lett. 1 (1) (2019) 147–153.

[18] F. Lucci, A. Della Torre, J. von Rickenbach, G. Montenegro, D. Poulikakos, P.D. Eggenschwiler, Performance of randomized Kelvin cell structures as catalytic substrates: mass-transfer based analysis, Chem. Eng. Sci. 112 (2014) 143–151.

[19] N. Kovacev, O. Doustdar, S. Li, A. Tsolakis, J.M. Herreros, K. Essa, The synergy between substrate architecture of 3D-printed catalytic converters and hydrogen for low-temperature aftertreatment systems, Chem. Eng. Sci. 269 (2023) 118490.

[20] R.K.A. Al-Rub, O.G. AL-KETAN, Catalytic converter substrates comprising triply periodic minimal surfaces, 2022, US Patent 11,286,831.

[21] M. Iwaniszyn, K. Sindera, J. Maszybrocka, P.J. Jodłowski, 3D-printed triply periodic minimal surface (TPMS) structures as catalyst carriers, Chem. Eng. Res. Des. 209 (2024) 37–51.

[22] O.H. Laguna, P.F. Lietor, F.J.I. Godino, F.A. Corpas-Iglesias, A review on additive manufacturing and materials for catalytic applications: milestones, key concepts, advances and perspectives, Mater. Des. 208 (2021) 109927.

[23] C. Busse, H. Freund, W. Schwieger, Periodic open cellular structures (POCS) as catalyst support for intensified heat transport in the partial oxidation of methanol to formaldehyde, Chem. Eng. J. 489 (2024) 151139.

[24] F. Mehdipour, C. Klahn, R. Dittmeyer, Multidisciplinary design analysis for washcoating of additively manufactured metallic monoliths, Procedia CIRP 128 (2024) 478–483.

[25] F. Agueniou, H. Vidal, J. de Dios López, J.C. Hernández-Garrido, M.A. Cauqui, F.J. Botana, J.J. Calvino, V.V. Galvita, J.M. Gatica, 3D-printing of metallic honeycomb monoliths as a doorway to a new generation of catalytic devices: the Ni-based catalysts in methane dry reforming showcase, Catal. Commun. 148 (2021) 106181.

[26] O. Bazta, F.J. Botana, J.J. Calvino, M.A. Cauqui, J.M. Gatica, H. Vidal, L. González-Rovira, J. López-Castro, M.P. Yeste, G. Blanco, et al., Novel combination of 3D-printing and electrochemical deposition to design and prepare metallic honeycomb supported catalysts for dry reforming of methane, Chem. Eng. J. 506 (2025) 159939.

[27] F. Grinschek, A. Charles, A. Elkaseer, C. Klahn, S.G. Scholz, R. Dittmeyer, Gas-tight means zero defects-design considerations for thin-walled fluidic devices with overhangs by laser powder bed fusion, Mater. Des. 223 (2022) 111174.

[28] J. Bear, Dynamics of Fluids in Porous Media, Courier Corporation, 2013.

[29] S.J. Cooper, D.S. Eastwood, J. Gelb, G. Damblanc, D. Brett, R.S. Bradley, P.J. Withers, P.D. Lee, A.J. Marquis, N.P. Brandon, et al., Image based modelling of microstructural heterogeneity in LiFePO4 electrodes for Li-ion batteries, J. Power Sources 247 (2014) 1033–1039.

[30] T. Delrieux, M.E. Ludwig, J. Czechowsky, P. Dolcet, F. Maurer, M. Casapu, J.-D. Grunwaldt, Toward automated catalyst preparation of monolithic honeycombs for ammonia oxidation by robot-Controlled washcoating, Emiss. Control Sci. Technol. 12 (1) (2026) 8.

[31] S. Tomin, K. Keller, U. Wagner, P. Lott, T. Koch, O. Deutschmann, Innovative engine test bench set-up for testing of exhaust gas aftertreatment and detailed gas species analysis for CNG-SI-operation, Automot. Engine Technol. 9 (1) (2024) 2.

[32] R.M. Heck, R.J. Farrauto, S.T. Gulati, Catalytic Air Pollution Control: Commercial Technology, John Wiley & Sons, 2016.

[33] Robert Bosch GmbH, Bosch Automotive Handbook, SAE International, 2018.